POLITECNICO DI TORINO

FACULTY OF ENGINEERING

Master’s degree in environmental and Territorial Engineering, Specialization: Industrial Environmental Sustainability

Master's Thesis

Flow field measurements around agrivoltaic PV module arrays: a flume similarity study.

Tutor: Professor Davide Poggi

Co-tutor: Ing. Elia Buono

Candidate:

Filippo De Miccolis Angelini

Academic year: 2025-2026

ABSTRACT

This study examines how photovoltaic (PV) panel arrays in agrivoltaics systems modify the structure of the atmospheric surface layer under near-neutral conditions. Experiments were performed in a recirculating flume channel equipped with 60 scaled PV panel models. Bed roughness representative of the crop layer was reproduced by uniformly distributing gravel along the channel bottom. Similarity with the full-scale configuration was ensured through Reynolds-number dynamic similarity.

A parametric campaign was carried out by varying panel inclination and flow rate. Three discharges were tested (0.035, 0.075, and 0.095 m^3/s), while the water depth at the upstream edge of the panel array was kept constant at 0.5 m for all cases. Panel inclination was investigated for four orientations (±20° and ±35°), where positive angles denote panels with the upper surface facing upstream and negative angles denote panels facing downstream, resulting in 12 configurations overall.

Velocity fields were measured using Particle Image Velocimetry (PIV). After preprocessing in DynamicStudio 8.4, the datasets were analysed in MATLAB to compute mean velocity components, turbulent kinetic energy, Reynolds stresses, and vorticity. These experimental results were then compared with predictions from Reynolds-Averaged Navier–Stokes (RANS) simulations. Overall, the findings show that the panel array substantially modifies the mean flow and turbulence characteristics, with the magnitude and spatial distribution of these effects strongly dependent on both panel inclination and flow rate.

LIST OF FIGURES

LIST OF TABLES

INDEX

INTRODUCTION

In recent years, the energy transition has emerged as one of the central topics in the global scientific and political debate. Ongoing population growth and the consequent increase in global energy demand make the development of renewable energy systems essential to mitigate greenhouse gas emissions associated with fossil fuel consumption.

Within this framework, photovoltaic technology plays a pivotal role due to its high versatility and simple installation requirements. The continuous reduction in production costs, combined with the steady improvement in module conversion efficiency, has led to the widespread deployment of photovoltaic plants, resulting in an increasing occupation of land areas.

However, while this expansion is crucial for achieving environmental sustainability targets, it also raises concerns related to land-use competition. The large surface areas required for panel installation may conflict with agricultural needs, making it necessary to rethink the integration between energy production and the preservation of agricultural land.

To address the challenges associated with land-use competition, research has increasingly focused on solutions capable of integrating energy production with pre-existing productive activities. Within this framework, agrivoltaics has emerged as a hybrid system designed to combine solar energy generation with agricultural practices on the same land surface.

The fundamental difference compared to conventional photovoltaic systems lies in the structural configuration and spatial arrangement of the modules. Traditional PV installations aim to maximize energy yield per unit area, typically through low-mounted and densely distributed panels, which effectively prevent agricultural use of the underlying land. In contrast, agrivoltaics systems are specifically designed to ensure the coexistence of energy production and crop

cultivation by employing elevated modules with greater spacing, thereby allowing sufficient solar radiation to reach the crops.

Several studies have investigated the effects of such configurations, highlighting the potential for synergistic benefits in both energy and agricultural performance. Among the most influential pioneering contributions is the work of Barron-Gafford et al. (2019), who, through experimental measurements conducted in arid environments, demonstrated that agrivoltaics systems can simultaneously enhance crop productivity, improve water-use efficiency, and maintain or even increase photovoltaic performance.

Subsequent studies have further investigated the microclimatic effects induced by the shading of photovoltaic panels. Weselek et al. (2021) analysed the impact of agrivoltaics systems on different crops under temperate climatic conditions, highlighting a reduction in photosynthetically active radiation (PAR) and soil temperature. Their findings revealed that crop responses are strongly dependent on both species-specific traits and interannual climatic variability.

Similarly, Campana et al. (2024), through experimental investigations conducted at northern latitudes, demonstrated that reduced solar irradiance does not necessarily lead to significant yield losses. In several cases, Land Equivalent Ratio (LER) values remained above unity, indicating a more efficient use of land resources compared to separate agricultural and photovoltaic systems.

Another important research stream focuses on crop physiological responses, particularly photosynthetic performance, and water stress mitigation. Recent work by Barron-Gafford et al. (2025) showed that partial shading provided by photovoltaic modules can alleviate the so-called midday depression of photosynthesis. This effect enhances daily carbon assimilation and improves plant resilience under conditions of elevated thermal stress, suggesting that agrivoltaics configurations may play a role in climate adaptation strategies.

Alongside the documented benefits, the literature also highlights limitations and practical challenges associated with agrivoltaics systems. Certain crops that are particularly sensitive to reductions in solar radiation, such as rice, may experience significant decreases in yield and quality under shaded conditions. This has been reported, for instance, by Thum et al. (2025), who emphasized the need for agrivoltaics designs specifically tailored to crop species and local climatic contexts.

Within this framework, the present thesis is part of a broader research project aimed at investigating how panel spacing and inclination influence the flow field developing around photovoltaic structures.

More specifically, this study focuses on the fluid dynamic phenomena occurring in proximity to the panels, as well as in the fluid regions above and below them along the vertical axis. Attention is devoted to the modification of the velocity field induced by geometric configuration parameters.

The layout analysed in this work is intended to provide a benchmark solution for subsequent investigations. The examined configuration, characterized by reduced spacing between modules, is structurally comparable to a conventional photovoltaic installation. For this reason, it represents a suitable reference case against which future agrivoltaics configurations—with larger inter-row distances and elevated mounting systems—can be systematically assessed.

1. LITERATURE REVIEW AND THEORICAL BACKGROUND

1.1 Laboratory experiments- state of art

This chapter aims to provide a structured and critical review of the current state of art concerning laboratory-scale experimental studies on agrivoltaics systems. Attention is devoted to experiments conducted in recent years, to establish a solid and up-to-date reference framework for the present work.

The following sections describe three significant experimental investigations that are particularly relevant to the objectives of this thesis.

1) Wind field characteristics of photovoltaic arrays based on wind tunnel tests – Meilin Li et al., 2025, Solar Energy:

The study conducted by Meilin Li et al. (2025) aimed to experimentally investigate the influence of a photovoltaic (PV) array on the surrounding airflow under incident wind conditions. Wind tunnel experiments were conducted using a uniform inlet velocity profile, while varying the wind attack angle to simulate different inflow directions. The analysed array was designed to replicate a photovoltaic power plant located in the Gobi Desert, China, ensuring geometrical and aerodynamic representativeness.

A scaled physical model of the PV array was installed inside the wind tunnel within controlled flow sections. Nine wind directions were considered, each tested under four different inlet velocity levels. The results demonstrated that the presence of the photovoltaic array significantly alters the atmospheric flow structure within the near-ground boundary layer.

At the array entrance, the incoming flow was partially deflected upward due to the blockage effect induced by the panels. Simultaneously, a pronounced wind acceleration was observed in the under-panel region. This acceleration was accompanied by the formation of localized recirculation zones and coherent vortical structures, particularly near the lower leading edge and the rear portion of the modules.

Within the array, the mean wind velocity was reduced compared to the undisturbed upstream flow. This attenuation became more pronounced at higher inlet velocities and for specific wind directions. The reduction effect was strongest near the ground and decreased rapidly with height, indicating that the disturbance induced by the panels is largely confined to the lower boundary layer.

Downstream of the array, the flow exhibited a gradual recovery of the original velocity profile; however, this reconstruction occurred over non-negligible characteristic lengths, highlighting the persistent aerodynamic influence of the installation. Wind direction emerged as a key parameter, with oblique inflow configurations generating more irregular and asymmetric velocity fields.

2) *Wind tunnel experiments on ground-mounted photovoltaic solar panels* – Javier López, Alberto Parnás & Pablo Cataldo, 2019:

This experimental study investigated the aerodynamic loads induced by wind pressure on ground-mounted photovoltaic panels—loads that are not yet fully addressed by existing design codes. To this end, rigid panel models with fixed tilt angles of 15° and 23° were tested in a wind tunnel environment.

The experimental results revealed that airflow interacts with the panels in a highly non-uniform manner. The measured pressure

distributions over the panel surfaces showed a strong dependence on both wind attack angle and module inclination. For frontal and rear wind conditions, high positive and negative pressure coefficients were observed, indicating flow separation phenomena and the formation of recirculation zones downstream of the panels.

An increase in module inclination led to a significant rise in aerodynamic loads, suggesting stronger flow disturbances and a more extended separation region. Although the study did not directly measure velocity fields, the pressure data clearly indicate that the panel behaves as an aerodynamic obstacle capable of deflecting the incoming flow, generating turbulence, and locally modifying the atmospheric velocity field.

These effects are especially relevant for configurations characterized by low ground clearance, typical of ground-mounted photovoltaic systems and, to some extent, certain agrivoltaics layouts.

3) *Dust deposition characteristics on photovoltaic arrays investigated through wind tunnel experiments* – Juan Wang et al., 2025:

The study conducted by Wang et al. (2025) aimed to investigate, through wind tunnel experiments, how key installation parameters of photovoltaic arrays—namely tilt angle, ground clearance, inter-row spacing, and wind direction—affect dust accumulation and particle distribution on panel surfaces. This issue is particularly critical in desert regions, where soiling not only reduces energy efficiency but also interacts with and reflects modifications of the local flow field.

The experimental setup consisted of an array of four identical panels exposed to an air–dust flow within a controlled wind tunnel environment. At the end of each test, the total deposited dust mass

and the particle size distribution were measured for each panel, as a function of both geometric configuration and wind direction.

The results showed that dust deposition patterns are closely linked to the airflow modifications induced by the panels. The first panel directly exposed to the incoming flow systematically exhibited the highest dust accumulation. This behaviour was attributed to the abrupt wind deceleration and the formation of recirculation zones upstream and immediately downstream of the leading module, which promote particle sedimentation. Within the array, the aerodynamic interaction between successive panels led to a highly non-uniform redistribution of particles, reflecting a heterogeneous and complex flow structure.

Both the amount and granulometry of deposited dust varied significantly with panel inclination, ground clearance, and inter-panel spacing. Reduced spacing intensified aerodynamic interactions between modules, whereas distances exceeding approximately twice the panel height mitigated mutual interference, indicating a partial recovery of the undisturbed flow between consecutive rows.

Overall, the findings demonstrate that the geometric configuration of a photovoltaic array directly governs the structure of the local flow field, influencing not only particle transport and deposition processes but also near-ground exchange mechanisms. These aspects are particularly relevant in agrivoltaic systems, where aerodynamic behaviour can affect both microclimatic conditions and crop performance.

1.2 Theoretical background

The aim of this work is to analyse how the presence of photovoltaic panels influences the airflow field within the lowest layers of the atmosphere. Attention is devoted to the phenomena developing inside the Atmospheric Boundary Layer (ABL).

The Atmospheric Boundary Layer represents the lowest portion of the atmosphere, extending from a few meters above the ground up to heights on the order of 1–2 km, depending on atmospheric conditions and thermal stability (Stull, 1988). Within this layer, airflow is strongly affected by multiple factors, including Earth's rotation (Coriolis forces), diurnal surface heating cycles, evolving meteorological conditions, and frictional forces exerted by the surface.

The combined action of these effects results in turbulent flow regimes. For modelling purposes, the ABL is commonly approximated as a turbulent boundary layer developing over a horizontally homogeneous solid surface. This assumption is considered appropriate when the analysis is restricted to the lower portion of the ABL and to conditions of horizontal homogeneity and thermal neutrality, under which atmospheric stability effects can be neglected.

This modelling approach is further justified by the very high Reynolds numbers that characterize atmospheric flows. The Reynolds number is defined as: $Re = \frac{\rho u L}{\mu}$, where ρ is the fluid density, u is a characteristic velocity, L is a representative length scale of the flow, and μ is the dynamic viscosity. In the atmospheric boundary layer, the Reynolds number typically reaches very large values, indicating that inertial forces largely dominate over viscous forces. Consequently, the flow regime is fully turbulent, and its structure can be described using theoretical frameworks derived from turbulent boundary layer theory.

Under such high-Reynolds-number conditions, velocity gradients in the direction perpendicular to the ground are much stronger than those in the streamwise direction. This implies that momentum transfer is primarily controlled by vertical shear stresses generated by the interaction between the airflow and the underlying surface. Therefore, the dominant physical mechanism governing the near-surface region is shear-driven turbulence production rather than viscous diffusion.

Assuming air behaves as a Newtonian and weakly compressible fluid, its motion can be described, to a first approximation, by the incompressible Navier–Stokes equations, suitably adapted for the modelling of turbulent atmospheric flows. These equations express the fundamental principles of conservation of mass and conservation of momentum.

The conservation of mass is given by the continuity equation:

$$\frac{\partial u_i}{\partial x_i} = 0 \quad (1.2.1)$$

In this expression, u_i denotes the instantaneous velocity component in the i-th spatial direction, while x_i represents the corresponding spatial coordinate. The operator $\frac{\partial}{\partial x_i}$ indicates a partial derivative with respect to x_i, meaning that the variation of the velocity component is evaluated while keeping the other spatial variables constant.

The subscript i follows the index notation commonly adopted in fluid mechanics and turbulence theory. According to Einstein summation convention, repeated indices imply summation over the three spatial directions (i = 1, 2, 3), corresponding respectively to the streamwise, vertical, and spanwise directions. Therefore, Eq. (1.2.1) compactly expresses the condition that the divergence of the velocity field is zero, ensuring mass conservation under incompressible flow conditions.

The conservation of momentum is described by:

$$\rho\left[\frac{\partial v_i}{\partial t} + v_j * \frac{\partial v_i}{\partial x_j}\right] = -\frac{\partial p}{\partial x_i} + \mu\frac{\partial^2 v_i}{\partial x_j^2} + \rho f_i \quad (1.2.2)$$

In this equation, ρ represents the fluid density, p is the pressure field, μ is the dynamic viscosity, and f_i denotes body forces per unit mass, such as gravity. The term $\frac{\partial u_i}{\partial t}$ represents local acceleration, while $u_j\frac{\partial u_i}{\partial x_j}$ accounts for convective acceleration, describing how momentum is transported by the motion of the fluid itself. The term $-\frac{\partial p}{\partial x_i}$ represents the effect of pressure gradients, $\mu\frac{\partial^2 u_i}{\partial x_j^2}$ describes viscous diffusion of momentum, and ρf_i accounts for external body forces acting on the fluid.

Together, equations (1.2.1) and (1.2.2) provide a complete mathematical description of the instantaneous motion of a Newtonian fluid. However, within the Atmospheric Boundary Layer, the direct application of these equations presents significant challenges. Atmospheric flows are characterized by very high Reynolds numbers and by the presence of turbulent structures spanning a wide range of spatial and temporal scales. Although the Navier–Stokes equations remain formally valid, their direct solution in terms of instantaneous flow quantities would require resolving all turbulent fluctuations, which is generally impractical. For this reason, a statistical averaging procedure is introduced in the following section, leading to the Reynolds-Averaged Navier–Stokes (RANS) formulation.

To render the problem tractable from a modelling standpoint, the Reynolds decomposition is introduced (Pope, 2000). This methodological approach consists of decomposing each instantaneous variable into two distinct components: a time-averaged (mean) contribution and a fluctuating contribution.

As an illustrative example, the decomposition of the velocity component u can be expressed analytically as: $u = \bar{u} + u'$, where $\bar{u}$ represents the time-averaged value over the considered interval, while u' denotes the fluctuating component associated with turbulent motions in the flow field.

Based on this decomposition, the conservation equations for mass and momentum can be reformulated. By substituting the instantaneous variables in the Navier–Stokes equations and in the continuity equation with their corresponding mean and fluctuating components, and subsequently applying the time-averaging operator, the Reynolds-Averaged Navier–Stokes equations (RANS) are obtained.

These equations describe the evolution of the mean flow field while incorporating the effects of turbulent fluctuations on the macroscopic fluid dynamics. By applying Reynolds decomposition and performing time averaging, the Navier–Stokes equations are reformulated into the Reynolds-Averaged Navier–Stokes (RANS) equations.

The continuity equation for the mean flow becomes:

$$\frac{\partial \overline{u_i}}{\partial x_i} = 0 \quad (1.2.3)$$

where $\bar{u_i}$ denotes the time-averaged velocity component in the i-th spatial direction.

The corresponding momentum equation reads:

$$\rho \left[\frac{\partial \bar{v_i}}{\partial t} + \overline{v_j} * \frac{\partial \bar{v_i}}{\partial xj}\right] = -\frac{\partial \bar{p}}{\partial xi} + \mu * \frac{\partial^2 \bar{v_i}}{\partial xj^2} - \frac{\partial}{\partial xj}(\rho \overline{v'_i v'_j}) + \rho f_i \quad (1.2.4)$$

In this formulation, the overbar indicates time-averaged quantities, while the primed terms u_i' represent velocity fluctuations with respect to the mean value. The first terms on the left-hand side describe the evolution and convection of the mean velocity field. On the right-hand side, the pressure gradient, viscous diffusion, and body force terms

retain the same physical meaning as in the instantaneous Navier–Stokes equations.

However, an additional term now appears:

$$\frac{\partial}{\partial xj}(\rho\overline{v'_\iota v'_J}) \quad (1.2.5),$$

which does not exist in the original instantaneous formulation. This term arises from the interaction between fluctuating velocity components and represents the divergence of the Reynolds stress tensor.

The quantity $-\rho\overline{v'_\iota v'_J}$ embodies the apparent stresses generated by turbulent fluctuations and accounts for the additional transport of momentum induced by turbulence. Physically, it represents the mechanism through which velocity fluctuations redistribute momentum within the flow. The introduction of this term gives rise to the well-known closure problem in RANS modelling, since the Reynolds stresses involve unknown correlations of fluctuating quantities that must be modelled rather than directly computed (Wilcox, 2006).

Within the present experimental configuration, the objective is to approximate the characteristics of the Atmospheric Boundary Layer by reproducing near-neutral atmospheric conditions. Under such a regime, buoyancy effects are considered negligible, implying that air parcels do not experience spontaneous vertical displacements due to density stratification.

Thermal stratification is therefore neglected, and a vertically uniform temperature profile is assumed throughout the flow domain. Furthermore, given the reduced spatial scale of the experimental setup, the influence of the Coriolis force and Earth's rotation can be disregarded, as they are not significant for the agrivoltaics and photovoltaic configurations

2. DESCRIPTION OF THE EXPERIMENT SETUP

2.1 Description of the experiment and its aim

The objective of the experiment is to assess how the presence of solar panels, arranged in agrivoltaics configurations, influences the characteristics of the atmospheric flow field. The experimental activity was carried out in a free-surface channel, where scaled panel models with a height of 10 cm were installed. To realistically reproduce the aerodynamic resistance and surface roughness typical of cultivated soil, the channel bed was covered with a gravel layer.

The validity of the scaled model with respect to real-world conditions is ensured by the principle of dynamic similarity based on the Reynolds number. By preserving both geometric and dynamic similarity between the model and the prototype, it is possible to faithfully reproduce the fluid dynamic phenomena observed under full-scale conditions.

The experimental campaign was conducted by systematically varying two key parameters: the inclination of the photovoltaic modules and the flow rate. Specifically, three flow rates were investigated: 0.035, 0.075, and 0.095 m^3/s. Regarding panel inclination, four configurations were analysed, pairing the panels according to their orientation with respect to the incoming flow (upstream- or downstream-facing). The adopted tilt angles were ±20° and ±35°, where the positive sign indicates inclination toward the upstream direction and the negative sign toward the downstream direction.

Experimental data acquisition was performed using the Particle Image Velocimetry (PIV) technique. This methodology relies on a laser sheet to illuminate tracer particles (seeding) dispersed within the fluid, enabling

the acquisition of high-resolution image sequences. By analysing particle displacement between consecutive frames, the velocity field of the fluid can be reconstructed, allowing for a detailed investigation of the developing flow phenomena.

Overall, the experimental campaign produced 24 acquisitions, corresponding to six measurements for each panel inclination (i.e., two for each considered flow rate). After preliminary image processing using Dynamic Studio 8.4, the data were exported to MATLAB for statistical analysis of the flow field. The horizontal and vertical mean velocity components, turbulent kinetic energy, Reynolds stresses, and vorticity were computed.

These quantities were subsequently represented graphically to evaluate the observed phenomena and were then compared with results obtained through numerical modelling based on the solution of the Reynolds-Averaged Navier–Stokes equations (RANS).

2.2 Description of the experimental channel

The experiment was conducted in a free-surface channel, employed as an experimental facility configured to reproduce the main fluid dynamic mechanisms typical of the atmospheric boundary layer developing over an array of solar panels.

The overall system configuration, illustrated in Figure 1, includes the arrangement of the scaled panel models, the gravel-covered bottom surface used to simulate ground roughness, and the designated measurement section for data acquisition.

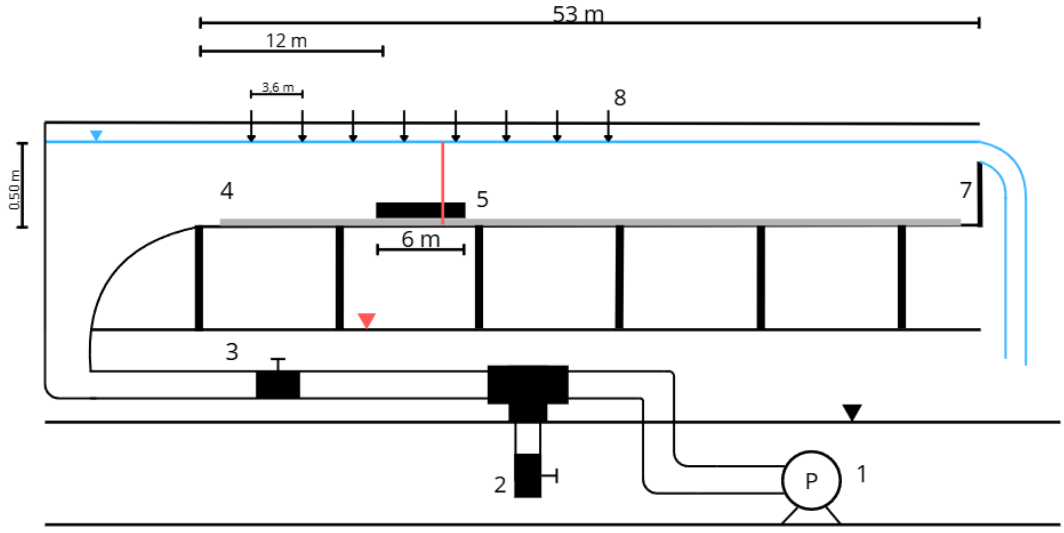

Figure 1: Schematic layout of experimental hydraulic channel. (1) pump; (2) bypass valve; (3) delivery valve; (4) gravel layer; (5) panel arrangement in the test section; (7) outlet gate; (8) verniers. The main geometrical dimensions of the channel are also reported.

Figure 2: Experimental hydraulic channel section with gravel layer placed on channel bed and support structures used for the verniers.

The system is powered by a pump (1), which ensures the required discharge within the channel. To achieve proper flow regulation, the hydraulic circuit is equipped with two control valves:

- The bypass valve (2), used to partially divert the flow to prevent overpressure and ensure system stability.
- The delivery valve (3), which regulates the flow rate directly supplied to the channel.

The channel has a total length of 53 m, with a cross-section 0.60 m wide and 0.80 m high. To reproduce the surface roughness typical of

agricultural terrain with low vegetation, a gravel layer (4) was installed along the bottom, corresponding to an equivalent roughness height of 0.10 m. This roughened section extends for 50 m, starting 1.5 m downstream of the inlet section, to allow the development of a fully developed boundary layer before the test area.

The section containing the scaled solar panel models (5) is located 12 m downstream of the channel inlet.

Figure 3: Arrangement of inclined panels installed in the test section on the gravel layer.

This arrangement, extending over a total length of 6 m, represents the core of the experimental setup. Each scaled panel model has a height of 10 cm and a width comparable to that of the channel, to occupy the entire transverse section. A total of 60 modules were constructed: 57 entirely made of stainless steel, while the three panels positioned at the measurement window (6) were manufactured with a glass surface.

This material difference is specifically required for the application of the Particle Image Velocimetry (PIV) technique. The measurement system employs a laser sheet to illuminate the flow field; therefore, the glass panels allow the laser beam to pass through without obstruction, enabling the camera to capture clear images across the entire measurement section.

The measurement area, indicated by number (6), has a length of approximately 15 cm and is highlighted in the general layout with a distinct colour to distinguish it from the surrounding modules.

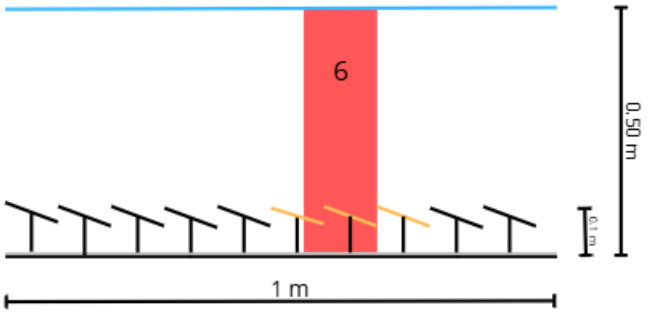

Figure 4: Schematic representation of the PIV acquisition region (6). The red region corresponds to the 15 cm illuminated by the laser.

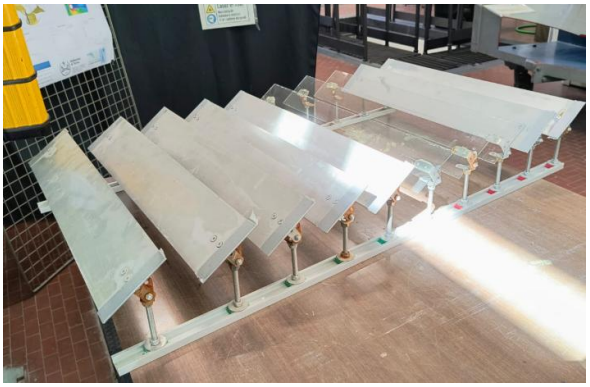

Figure 5: Inclined panels used in the experiments, mounted on an adjustable support structure to set the desired inclination angle.

The bottom of the measurement section is made of transparent material to allow proper illumination of the flow field by the laser sheet. Specifically, the structure consists of three superimposed layers (from bottom to top): a lower glass panel positioned directly above the laser source, an intermediate air gap, and an upper plexiglass panel. The latter is equipped with a dedicated optical opening designed to ensure undisturbed light transmission.

Attention was devoted to maintaining high image quality during data acquisition. During the experimental runs, suspended sediments

present in the gap tend to deposit on transparent surfaces, potentially attenuating or refracting the laser beam. To mitigate this issue, an internal cleaning system was designed, consisting of a brush and a cloth mechanism. These elements are actuated externally by means of a magnet, allowing rapid and effective removal of impurities from both the glass and plexiglass surfaces without interrupting the experimental setup.

Figure 6: Brush used to clean the optical window on the plexiglass panel (up) and the cloth to clean the glass panel (down). The cleaning system is externally actuated by a magnet, allowing the removal of sediment deposits.

At the downstream end of the channel, a sluice gate (7) is installed to regulate the water level. This component is essential for ensuring stable operating conditions throughout the experiment, as the water depth must be maintained at a nominal value of approximately 50 cm.

Variations in discharge naturally lead to changes in the water level; however, the desired depth can be restored by manually adjusting the control handle of the sluice gate. This regulation system allows precise control of the hydraulic boundary conditions, ensuring repeatability and consistency across different experimental runs.

Figure 7: Outlet gate used to control the downstream water level in the hydraulic channel.

The free-surface profile is measured using eight vernier gauges (8). A vernier consists of a sliding auxiliary scale used in combination with a main scale to accurately measure fractions of a millimetres. The measurement is obtained by identifying the line on the vernier scale that aligns with a corresponding mark on the main scale, allowing intermediate values between two primary divisions to be determined with high precision.

In the present setup, the vernier gauges are positioned along the channel starting 3.6 m downstream of the inlet section, with a constant spacing of 3.6 m, extending up to 28.8 m downstream, as shown in the schematic layout. In particular, the fourth vernier, located 14.4 m downstream, is used as the fixed reference for water level calibration. This reference point ensures consistency and repeatability of the hydraulic boundary conditions throughout the entire experimental campaign.

2.3 Procedure of channel's activation

Before performing any data acquisition, the channel must first be filled with water. This operation requires a strict procedural sequence to ensure the integrity of the experimental configuration and the safety of the hydraulic system.

The operational procedure consists of the following steps:

1. Valve inspection: Prior to activating the pump, the valve configuration must be carefully checked. The bypass valve must be fully open, while the delivery valve must be completely closed. This step is essential to prevent excessive hydraulic load on the delivery valve during system start-up.
2. Pump start-up: Once the valve configuration has been verified, the pump can be switched on using the designated control switch, and the flow meter must be activated. The flow meter allows continuous monitoring of the discharge supplied to the channel, ensuring that the imposed flow rate corresponds to the desired value and preventing excessive water input during the initial filling phase.
3. Initial channel filling: After the pump has been started, the delivery valve can be gradually opened by approximately 7–10 turns. This controlled adjustment allows a limited amount of water to enter the channel, preventing the generation of excessive velocities that could induce undesirable drag effects on the experimental setup.

   The mean flow velocity is calculated as:

$$V_{avg} = \frac{Q}{h*d*1000} \quad (2.3.1)$$

where Q is the discharge, d is the channel width, and h is the free-surface height.

During the initial filling phase, the water depth is relatively low. Consequently, introducing an excessive discharge may result in high flow velocities, potentially damaging the internal configuration of the channel. For this reason, it is essential to maintain sufficiently low velocities at this stage, specifically below 0.25 m/s.

4. Filling of the air gap: When the water level reaches approximately 5 cm at the location of the delivery valve, the flow is temporarily interrupted by closing the valve. This step is essential to prevent undesired disturbances in the measurement region. Beneath this area, an air-filled cavity (air gap) is present at the beginning of the procedure. If the filling process were too rapid, air bubbles could form and become trapped, potentially compromising the stability of the glass panel arrangement. A controlled interruption of the flow ensures gradual filling of the cavity and safe air evacuation.
5. Channel filling to operating discharge: Once the air gap has been filled and all entrapped air has been progressively released, the filling process can resume until the desired discharge is reached. This operation must be carried out gradually, opening the delivery valve by 10–15 turns at a time to allow the water level to rise smoothly and avoid abrupt hydraulic variations.

   When the delivery valve is fully open (corresponding to $Q = 18\,\mathrm{L/s}$), further increases in discharge are achieved by progressively closing the bypass valve. During this phase, the magnetic cleaning system previously described is also activated

to remove any sediment deposits from the transparent surfaces, ensuring optimal optical conditions for measurements.

6. Water level stabilization: After the target discharge has been reached, the final step consists of fine adjustment of the downstream sluice gate. This regulation allows the free surface to be stabilized at the nominal elevation required for the experimental runs, thereby ensuring steady and repeatable hydraulic conditions.

2.4 Procedure for the choice of the seeding

A crucial aspect for the quality of Particle Image Velocimetry (PIV) acquisitions is the selection of the seeding particles, i.e., the tracer particles used to make the flow field visible. The ideal tracer must exhibit strong light-scattering properties to be clearly detectable during image analysis, while simultaneously having a density close to that of the working fluid to ensure accurate hydrodynamic tracking of the flow motion.

To guarantee a correct and uniform release of the tracer within the channel, a 10 L tank was employed. Before each acquisition, the tank was filled with a mixture of water and seeding particles. An internal mechanical stirrer was installed inside the tank to prevent particle flotation or sedimentation and to ensure the most homogeneous possible distribution during injection into the flow.

The seeding is introduced into the channel through a series of small tubes connected to the outlet valve of the tank and fixed to a metallic rod. The tube outlets are positioned at different vertical elevations to promote a uniform release of tracer particles across the entire depth of the channel.

The location of the tank relative to the measurement section was determined according to two main criteria. On the one hand, the distance could not be excessive, to prevent sedimentation or excessive dispersion of the tracer before reaching the acquisition area. On the other hand, it could not be too short, to ensure complete mixing of the seeding particles prior to entering the measurement section.

To optimize this positioning, mixing distances were evaluated both in the vertical and transverse directions for the different tested discharge values.

Flow (L/s)	Vml (m)	Tml (m)
95	1.24	2.66
75	0.98	2.10
35	0.46	0.98

Table 1: Mixing length values calculated for different flow rates. "Vml" and "Tml" refer respectively to the vertical and transverse mixing lengths.

Since the maximum calculated distance required for complete mixing was equal to 2.66 m, the tank was positioned approximately 5.5 m upstream of the measurement section, thus providing a sufficient safety margin to ensure proper seeding homogenization before reaching the acquisition area.

Figures 8 and 9 below show the detailed layout of the adopted configuration, including the arrangement of the injection system and the nozzle distribution used for tracer release.

Figure 8: Seeding system used to introduce tracer particles into the flow for the PIV measurements.

Figure 9: 4 nozzles at different height used to inject tracer particles into the flow for the PIV measurements.

Regarding the selection of the seeding material for the experimental campaign, three different tracer types were evaluated:

- Hollow Glass Silver Coated (dp = 10 μm): Hollow glass microspheres coated with silver, characterized by high reflectivity. While they provide strong optical response, they may be susceptible to attenuation effects in turbid media.
- Kaolin (dp = 5.5 μm): A fine mineral powder with very small particle size, ensuring high hydrodynamic fidelity due to its low inertia. However, its optical response is generally weaker compared to coated or polymeric particles.
- Polyamide (PSP) (dp = 20 μm): Polymeric particles with irregular shape and larger diameter, offering increased reflective surface area and potentially improved visibility in less clear water conditions.

To assess the performance of the different tracers, dedicated acquisition tests were carried out. For each case, 120 images were recorded at an acquisition frequency of 1 Hz. Using the Particle Density tool within the Particle Image Velocimetry processing workflow, the

particle concentration inside the interrogation areas (IA) was quantified at different vertical positions in the flow field.

Seeding	Quantity (ml)	C down (Np/px²)	C middle (Np/px^2)	C up (Np/px^2)	C mean (Np/px^2)
No seeding	0	45.00	58.50	27.33	43.61
Hollow glass	5	51.67	99.00	28.00	59.56
Kaolin	20	159.00	221.00	78.33	152.78
Polyamide	10	112.67	197.00	76.33	128.67

Table 2: Results of the seeding analysis for different tracer particles and injected quantities. "C" values represent the particle concentration measured at different channel *positions.*

As shown in Table 2, although kaolin exhibited the highest particle density along the entire vertical profile, the final selection fell on polyamide particles.

This decision was based on two key considerations. First, polyamide provides superior optical contrast compared to hollow glass particles, thereby facilitating velocity vector processing and improving the robustness of the correlation algorithm in the Particle Image Velocimetry analysis. Second, unlike kaolin, polyamide does not induce significant turbidity in the working fluid, thus preserving optical clarity within the measurement section and ensuring more reliable image acquisition throughout the experimental campaign.

2.5 PIV description

Particle Image Velocimetry (PIV) is a non-intrusive measurement technique that enables the reconstruction of the instantaneous velocity field within a moving fluid (Raffel et al., 2018). It is based on the analysis of images acquired in rapid succession, capturing the motion of tracer particles dispersed in the flow.

Prior to acquisition, micrometric particles are added to the fluid. These particles are typically neutrally buoyant and have a density close to that of the working fluid, ensuring that they accurately follow the flow

trajectories. The measurement volume or plane is then illuminated by a laser beam, which generates a thin light sheet in which the particles become visible. Once the required image pairs have been acquired, the particle displacement between two consecutive frames is computed. Dividing this displacement by the time interval (Δt) between images yields the local fluid velocity field.

PIV is widely appreciated for its numerous advantages. It is non-intrusive, as it does not disturb the flow; it can provide two-dimensional or three-dimensional measurements; and it allows detailed investigation of transient and turbulent phenomena with high spatial and temporal resolution.

The experimental workstation consists of the following main components:

- Computer: Equipped with Dynamic Studio, which serves as the control interface for setting acquisition parameters, storing raw data, and processing image pairs to obtain the velocity field through cross-correlation analysis.
- Laser generator: Produces the laser beam required for illumination of the measurement plane. It is equipped with both a power switch and a safety key to ensure controlled activation.
- Control panel: Connected to the laser generator, it provides an additional safety layer. From this panel, the operator can activate the laser, open or close the shutter, and regulate the beam intensity according to the acquisition requirements.
- Laser sheet forming system: A set of cylindrical lenses transforms the laser beam into a thin light sheet, illuminating only the selected flow section. This configuration ensures that tracer particles within the measurement plane are clearly visible while

minimizing unwanted light scattering outside the region of interest.

- Acquisition cameras: Two high-resolution cameras are used for image acquisition. They are mounted on a dedicated support structure that allows precise adjustment of parameters such as distance and height relative to the channel, camera inclination, and focus across the entire measurement area. The cameras are connected to a synchronization unit that coordinates image capture with the laser pulses, ensuring accurate timing between illumination and recording.

3. DESCRIPTION OF THE ACQUISITION PROCESS

3.1 Calibration of the cameras

The camera calibration procedure represents a fundamental step in ensuring the methodological accuracy of the Particle Image Velocimetry (PIV) system. Calibration establishes a one-to-one correspondence between the pixel coordinates recorded by the camera sensors and the physical coordinates within the laser-illuminated measurement plane. In this way, each measured displacement can be correctly converted into real spatial quantities, preserving the spatial accuracy of the system.

To reproduce the actual light refraction conditions occurring during the experiments, calibration is performed with the channel filled with water. Using Dynamic Studio, a reference calibration grid is activated, and a preview acquisition is carried out. This preliminary step allows verification of both proper focus and the geometric alignment of the acquired scene.

To ensure correct centring of the objective within the grid, an auxiliary light source is used to assess lens positioning. Once proper alignment has been confirmed for both cameras, fine focusing is performed. The lens is adjusted until the tracer particles (seeding) appear sharply defined, ensuring that they are clearly distinguishable across the entire acquisition surface.

The final stage of calibration consists of defining the physical length scale in meters for the measurements. To accomplish this, a metal rod equipped with a graduated scale is placed inside the channel. After acquiring the corresponding images, three distinct reference points

along the ruler are selected. This procedure allows an unambiguous determination of the relationship between horizontal and vertical distances expressed in pixels and their corresponding values in millimetres, thereby completing the spatial scaling of the system.

3.2 Calibration of ultrasonic sensors and verniers

Another aspect requiring careful attention during the calibration phase concerns the vernier gauges and the ultrasonic sensors.

Regarding the vernier gauges, the procedure begins by establishing hydrostatic conditions inside the channel. This is achieved by sealing the channel with a metal plate and subsequently filling it to the desired calibration level (50 cm). Once the target water depth is reached, the free-surface elevation is measured using the vernier gauges. Typically, five to six measurements are performed: three taken from upstream to downstream and the remaining ones from downstream to upstream. This bidirectional approach minimizes the influence of unavoidable small volume losses within the channel, since a perfectly watertight seal cannot be achieved.

After collecting all measurements, the difference between the elevation recorded by each vernier and that measured by vernier number 4—used as the reference—is computed. Because each vernier is characterized by its own instrumental zero, which is not necessarily identical across devices, this normalization step is required to establish a consistent elevation reference system along the entire length of the channel.

The calibration of the ultrasonic sensors follows a different procedure. In this case, the channel is filled to a height of approximately 52 cm, using the graduated ruler positioned near the delivery valve as a reference. The readings provided by the four ultrasonic sensors are then recorded

in an Excel file. Subsequently, the free-surface level is progressively lowered. This process is repeated five times.

The collected data for each sensor are then used to perform a linear fitting analysis, allowing verification that the decrease in water level measured by the vernier gauge is consistent with that detected by the ultrasonic sensors. This comparison ensures coherence and reliability between the two independent measurement systems.

To verify the correctness of the calibration, the coefficient of determination, denoted as R^2, is computed. This parameter ranges from 0 to 1 and quantifies how well the linear model explains the variability of the measured data. A value equal to 1 indicates perfect agreement between the experimental measurements and the linear model, whereas values close to 1 indicate strong linearity and, consequently, accurate calibration.

In the present context, the calibration is considered valid only if R^2 falls within the interval 0.999–1.000. Meeting this requirement ensures that the calibration procedure has been properly carried out and that the experimental acquisitions can proceed under reliable measurement conditions.

Figure 10 below reports the results of the ultrasonic sensor calibration procedure.

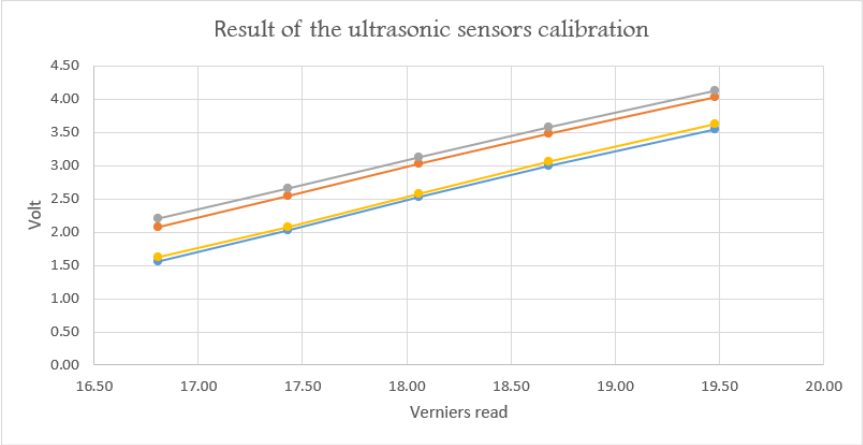

Figure 10: Calibration results of ultrasonic sensors used to measure the water level.

3.3 Description of the acquisition process

Once the calibration phase was completed, the experimental data acquisition was carried out. This stage requires a systematic and well-defined procedure to ensure repeatability and consistency across all tests.

- Channel setup: The first step involved configuring the hydraulic conditions of the channel. After setting the desired discharge for the acquisition, the air gap beneath the measurement section was cleaned using the magnetic system. Simultaneously, the seeding tank was filled with the water–tracer mixture.
- Camera activation: The acquisition cameras were switched on, followed by activation of the synchronization unit, which coordinates camera exposure with laser pulses.
- Laser activation: The laser generator was activated using the dedicated safety devices (key switch and interlock system). From the control panel, the laser was armed to initiate illumination of the measurement plane.

- Determination of Δt: Before starting the full acquisition, the time interval Δtbetween two consecutive images was determined. Two preliminary images were recorded to evaluate particle displacement. The displacement must fall within the range of 7–12 pixels to ensure accurate velocity field computation. This procedure was performed independently for both cameras.
- Seeding release: Once the appropriate Δt was identified, the tank valve was opened to introduce tracer particles into the channel.
- Image acquisition: After allowing approximately two minutes for the seeding to reach and homogenize within the measurement region, the acquisition of 3000 images was performed. The acquisition was repeated twice for each selected Δt value.
- Water level measurement: At the end of the acquisition process, the free-surface elevation was measured using both the vernier gauges and the ultrasonic sensors. Specifically, five measurements were taken with the verniers and one with the ultrasonic sensors.

Once all these steps were completed, the procedure was repeated for the next discharge value. The sluice gate was adjusted accordingly to regulate the water level, ensuring consistency and precision across successive acquisitions.

Figure 11 below presents the set of plots obtained from the water level measurements, highlighting the free-surface profiles for the different discharges and panel inclinations tested during the experimental campaign.

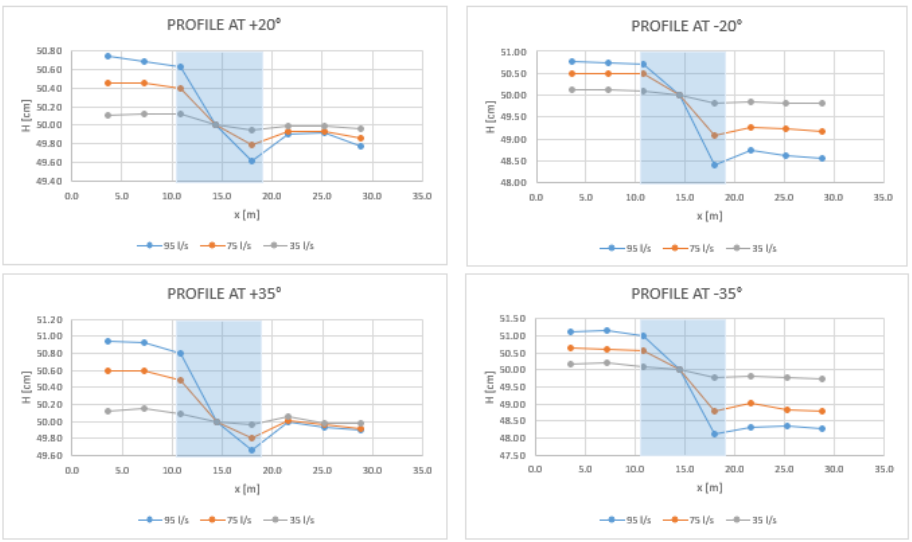

Figure 11: Vertical profiles of the hydraulic head for the investigated panel inclinations (+20°, −20°, +35°, −35°). Each subplot corresponds to a different angular configuration, while the curves represent the three analysed flow rates (35, 75, and 95 L/s). The shaded region highlights the streamwise location of the inclined panel within the channel.

4. DATA ANALYSIS PROCEDURE

4.1 Preliminary analysis of the images acquired

A fundamental step in obtaining reliable data through digital image processing consists of minimizing noise and unwanted disturbances within the acquired images. To achieve this, background removal is required, i.e., the elimination of all extraneous elements that may interfere with accurate velocity field evaluation based on particle analysis. Such elements include the gravel bed, the scaled panel models, and impurities suspended in the water.

In Dynamic Studio 8.4, background subtraction can be performed using different processing tools. Before describing the procedure ultimately adopted, the alternative methods that were preliminarily tested are briefly discussed.

The first tool evaluated was *Image Math*. However, this approach proved unsuitable for the intended purpose, as it operates on individual images only. Consequently, the results obtained did not meet the required quality standards for robust flow field reconstruction. For this reason, the analysis proceeded using the *Image Arithmetic* tool, which allows more advanced and consistent background subtraction across image sequences.

In this case, the adopted processing workflow consists of two distinct steps:

- Determination of the minimum-intensity image over a selected acquisition interval.

- Use of this image containing primarily noise and background elements as a subtraction operator through the *Image Arithmetic* tool.

Unlike *Image Math*, the *Image Arithmetic* tool in Dynamic Studio allows the use of an external reference image as an operator for batch processing. The first step therefore consisted in generating the minimum-intensity image from the entire available image set using the *Image Min/Max* function. This function computes, pixel by pixel, the minimum intensity value across all frames, producing a resulting image that predominantly contains static elements associated with the background.

Once this reference image was generated, it was imported into the project workspace as an operator. Subsequently, the *Image Arithmetic* interface was accessed, the appropriate subtraction operation was selected, and the full image sequence was processed. This procedure enabled effective background removal, significantly improving particle visibility and enhancing the reliability of the subsequent velocity field computation.

However, this approach also exhibited certain limitations. During the experimental runs, the illumination conditions within the images varied over time. Consequently, the single minimum-intensity image computed from the full set of 3000 frames was not sufficiently adaptive to account for temporal light fluctuations. This reduced the effectiveness of the background subtraction process.

For this reason, the Dynamic Background Removal method available in Dynamic Studio was ultimately adopted. From a conceptual standpoint, this approach proved more suitable for handling illumination variability and, more generally, for overcoming the shortcomings encountered

with the previously tested techniques. However, the application of this tool requires, as a preliminary step, the computation of the Proper Orthogonal Decomposition (POD).

Proper Orthogonal Decomposition is an analysis technique that allows a complex flow field to be decomposed into a set of orthogonal modes, ranked according to their energy content. This decomposition makes it possible to identify the dominant flow structures and to separate the dynamically relevant signal components from contributions associated with background noise and static elements.

The POD analysis produces a sequence of images, referred to as POD modes. These modes represent both the mean flow information and the energetically less significant components, which are generally attributable to noise and background features. The appropriate modes are then selected and incorporated into the Dynamic Background Removal tool to enhance the efficiency of the background subtraction process.

Figure 12 below presents representative images illustrating the results obtained using the different background removal methods described above.

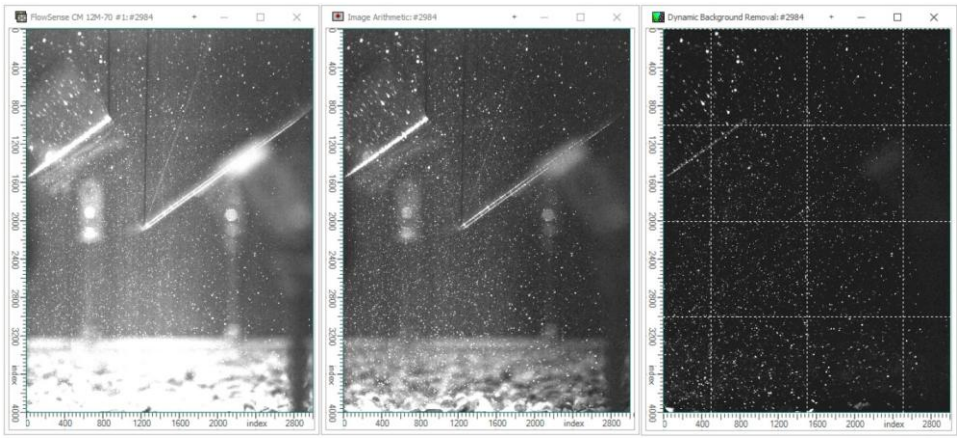

Figure 12: Comparison of PIV images obtained using different background removal methods: original image (left), image arithmetic (centre) and dynamic background removal (right).

To further verify the effectiveness of the background removal procedure, the entire process was replicated in MATLAB.

The first step consisted of automatically importing all images acquired by the Particle Image Velocimetry (PIV) system and organizing the frames into a single multidimensional matrix. This structure enabled consistent processing of the complete dataset and facilitated batch operations across the image sequence.

At this stage, it was necessary to convert the image format from *uint8* to *double*. Since MATLAB interprets images as numerical matrices, this conversion is essential to correctly perform arithmetic operations particularly subtraction while avoiding quantization errors.

To identify and isolate background elements, a minimum-intensity image was computed on a pixel-by-pixel basis. For each spatial location, the minimum intensity value across the selected image set was extracted. In this validation phase, the number of analysed frames ranged between 10 and 100, the choice of a reduced pull of images compared to the full dataset was done to limit computational cost and execution time, as this represented a preliminary test of the processing routine.

The subsequent subtraction of the background matrix from each original frame produced filtered images suitable for comparison with the results obtained using Dynamic Studio. This enabled both qualitative and quantitative assessment of the background removal effectiveness. Figure 13 below presents a representative example of the result obtained following this processing step.

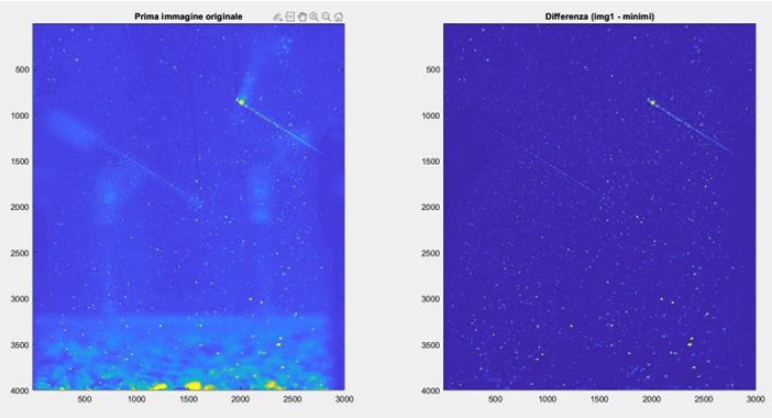

Figure 13: Result of the background removal performed in MATLAB. The original image is shown on the left, while the processed image after background subtraction is shown on the right.

Considering the results obtained from the comparative analysis, the Dynamic Background Removal method proved to be the most effective approach for background subtraction.

Compared to the previously tested techniques, it demonstrated superior adaptability to temporal illumination variations and provided a more consistent separation between meaningful flow information and static or noisy background components. Consequently, this method was selected for the final processing of the experimental image datasets.

4.2 Dynamic background removal and definition of the flow field

Once the preliminary analysis was completed and the optimal methodology identified, the background removal and subsequent reconstruction of the flow field were carried out. This procedure consists of four consecutive steps, performed entirely within Dynamic Studio 8.4. The first two steps are aimed at improving the quality of the acquired images. During the acquisition phase, the images are typically affected by the presence of several extraneous elements that may compromise accurate velocity field determination, such as the gravel bed and the

panels of the experimental model (Figure 14). These static features must be properly filtered out to enhance particle visibility and ensure reliable cross-correlation during velocity computation.

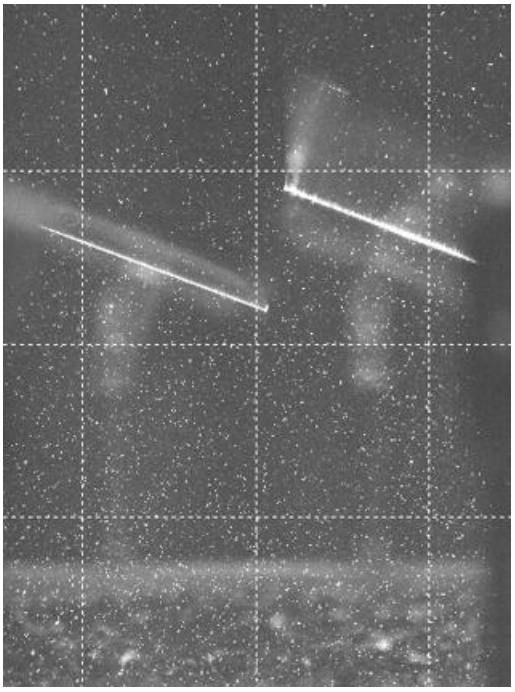

Figure 14: Example of a raw PIV image acquired during the experiments, showing the distribution of illuminated tracer particles in the measurement plane.

It is therefore necessary to perform an image-cleaning operation to enhance tracer particle visibility and reduce both background noise and stationary elements. To achieve this, the first step consists in computing the Proper Orthogonal Decomposition (POD) of the acquired image set. Proper Orthogonal Decomposition (POD) is an analysis technique that allows a complex flow field to be decomposed into a set of orthogonal modes ranked according to their energy content (Holmes et al., 1996).
The application of POD enables the decomposition of the image dataset into a series of orthogonal modes, each representing a coherent structure of the field from both spatial and temporal perspectives. In general, the fixed or slowly varying background is concentrated in the first modes, as it is characterized by high energy content and low temporal variability. The higher-order modes, by contrast,

predominantly contain the dynamic information associated with particle motion.

By excluding the first modes during image reconstruction, it is possible to effectively remove the stationary background components, resulting in images where the tracer particles are clearly highlighted and more suitable for accurate velocity field computation.

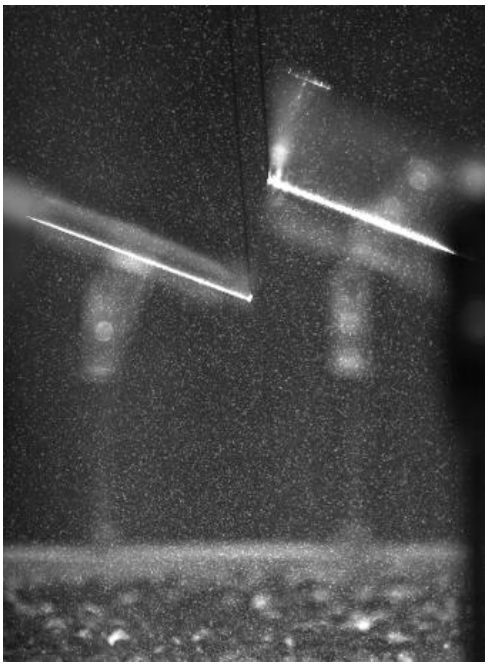

Figure 15: Example of a Proper Orthogonal Decomposition (POD) mode showing the principal elements in background (gravel, panel structure).

Once the POD modes had been generated, the actual image-cleaning phase was carried out. This requires selecting the POD set corresponding to the specific acquisition and subsequently launching the desired processing tool within Dynamic Studio.

During this step, the software requests the selection of the Modal Analysis images to be used as a reference for processing. This selection is automatically performed by Dynamic Studio according to the predefined parameters, allowing the background subtraction procedure to adapt to the specific conditions of each acquisition.

As shown in Figure 16, the resulting improvement in the signal-to-noise ratio significantly enhances the clear and unambiguous identification of tracer particles, thereby increasing the reliability of the subsequent velocity field reconstruction.

Figure 16: Example of a PIV image after background removal procedure, showing only the illuminated tracer particles.

Once the background removal was completed, the next step consisted of generating the velocity field, with the aim of extracting the different velocity components subsequently used for temporal and spatial statistical analysis.

For this purpose, the Adaptive PIV analysis tool available in Dynamic Studio (Dantec Dynamics) was employed. Adaptive PIV is an advanced technique for computing velocity fields from PIV image pairs, specifically designed to automatically adjust to local flow conditions. Its primary objective is to improve measurement accuracy and reliability compared to conventional PIV methods, particularly in the presence of strong velocity gradients, variations in particle density, image noise, and near-wall regions.

The method is based on an iterative cross-correlation scheme in which the interrogation areas (IA) are not kept fixed but are progressively modified in size, position, and shape. The analysis begins using the largest allowable IA size to obtain a robust initial estimate of particle displacement. In subsequent iterations, the IA size is locally reduced in regions where particle density is sufficiently high, thereby increasing the spatial resolution of the velocity field without compromising correlation quality.

The distribution of velocity vectors is defined by a regular grid, whose spacing determines the distance between adjacent vectors. If the grid spacing is smaller than the IA size, the interrogation areas may overlap, allowing a higher density of velocity vectors. The method also ensures that the minimum IA always remains within the analysis domain, while the maximum IA may extend beyond the image boundaries or the selected region of interest when necessary to preserve correlation robustness.

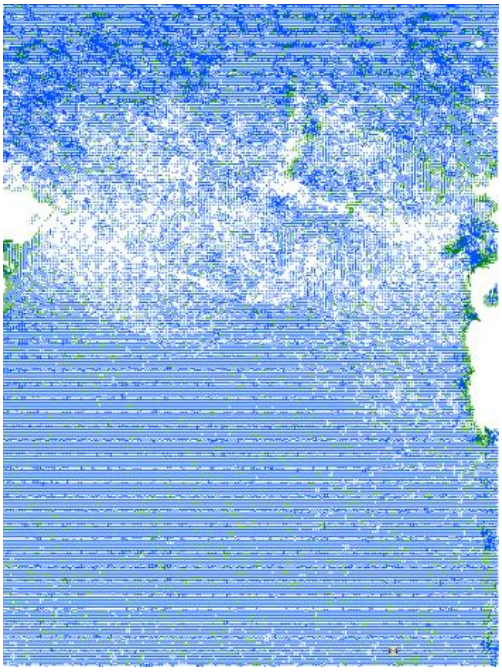

Figure 17: Example of a velocity vector field computed using the Adaptive PIV algorithm.

The procedure is completed with the application of the PIV Uncertainty module, aimed at providing a rigorous estimation of the uncertainty associated with each PIV displacement vector. This method evaluates the probability that the computed vector deviates from the true value, independently of the actual error, which remains intrinsically unknown. The uncertainty therefore defines a confidence interval for the measured velocity values and represents a fundamental tool for assessing the reliability of the results, particularly in complex flow conditions or in regions characterized by low tracer particle density.

One of the main approaches adopted for this estimation is based on the Peak Height Ratio (PHR) method proposed by Charonko and Vlachos (2013). This technique exploits the ratio between the primary correlation peak and the second highest peak obtained during the PIV cross-correlation process. A dominant primary peak indicates a reliable displacement vector, whereas peaks of comparable magnitude suggest ambiguity and higher uncertainty. The peak ratio is subsequently translated into an estimate of the radial error of the vector, representing the overall probability of deviation in the two-dimensional measurement space.

In summary, the Charonko & Vlachos method provides a practical and quantitative framework for associating each PIV vector with a reliability indicator derived solely from correlation statistics, without requiring knowledge of the true velocity field.

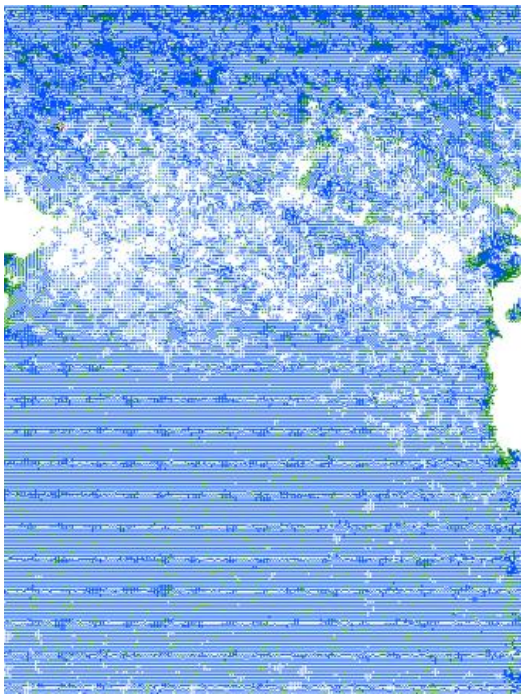

Figure 18: Example of velocity field obtained after the application of the PIV Uncertainty method.

At the end of the entire processing chain, the resulting images are stored in dedicated folders, each uniquely identified through a predefined naming convention.

This structured organization ensures systematic dataset management and proves essential for the subsequent stages of data analysis, facilitating traceability, repeatability, and efficient comparison between different experimental configurations.

4.3 Description of the MATLAB code for the roto-translation matrix

After completing the acquisition phase, it is necessary to compute the roto-translation matrix to merge the fields of view of the two cameras and determine the geometric transformation required to align them within a single reference system.

The procedure consists of the following steps:

1. Image Pre-processing: The acquired images were first converted to grayscale to simplify the extraction of relevant geometric features. Subsequently, they were converted to *double* numerical format to enable more accurate numerical processing and reduce quantization effects during computation.

2. Extraction of Characteristic Lines: The alignment between the two images is based on the identification of shadow cones and light cones generated during acquisition due to the interaction between the laser sheet and the panel edges of the experimental model. These features are clearly visible in both images and provide reliable geometric references for the alignment process.

For each image, three main reference lines were identified through the following steps:

- Thresholding: An intensity threshold was applied to isolate pixels belonging to the relevant lines from the background.
- Noise filtering: Small isolated regions were removed using morphological operations (e.g., *bwareaopen*) to eliminate spurious artifacts.
- Region of Interest (ROI) selection: The analysis was restricted to image portions containing the relevant line features, excluding peripheral non-informative areas.
- Linear fitting: A regression-based linear fit was applied to the selected pixels, determining the slope and intercept parameters for each line.

This procedure was applied to both the lower and upper images, resulting in two sets of line parameters, (a_{1m}, b_1) and (a_{2m}, b_2), for the three reference lines used in the alignment process.

3. Computation of the Geometric Transformation: To align the two images, a two-dimensional similarity transformation was adopted, combining rotation, scaling, and translation. The transformation parameters were determined by solving a linear system constructed from the parameters of the corresponding reference lines identified in the two images.

Specifically, for each line, the slope and intercept in the upper image were expressed as functions of the transformation applied to the corresponding line in the lower image. By imposing geometric consistency between corresponding lines, a linear system was obtained and subsequently solved to determine the unknown transformation parameters.

The solution of this system yields the fundamental components of the similarity transformation, described below:

- Scale factor s: This parameter represents the dimensional adjustment required for the lines in the two images to become congruent. It is computed as the norm of the first two coefficients of the linear system, which jointly contain information related to both rotation and scaling.
- Rotation angle θ: The rotation angle θdefines the angular displacement required to align the reference lines detected in the upper image with the corresponding lines in the lower image. It is computed from the coefficients of the linear system associated with the sine and cosine terms of the transformation.

  To improve numerical stability and reduce approximation errors, the final estimate of $\theta$is obtained by averaging the values derived independently from the inverse sine (arcsin) and inverse cosine (arccos) functions. This procedure mitigates potential

inaccuracies arising from rounding effects or local numerical sensitivity in the trigonometric inversion.

The corresponding two-dimensional rotation matrix is therefore expressed as:

$$R = \begin{bmatrix} \cos\theta & -\sin\theta \\ \sin\theta & \cos\theta \end{bmatrix} \quad (4.3.1)$$

This matrix represents the rotational component of the similarity transformation and describes a rigid rotation in the plane. When combined with the scale factor and the translation vector, it enables the geometric alignment of the two camera fields of view within a unified reference frame.

- Translation vector t: This parameter represents the displacement required along the X and Y axes to ensure coincidence between the corresponding lines once rotation and scaling have been applied.

The translation components are obtained directly from the remaining terms of the linear system solution. Once the scale factor and the rotation matrix have been determined, the complete similarity transformation between the two camera reference systems can be written as: $p_1 = s \cdot R \cdot p_2 + t$, where p_2 denotes the coordinates of a point in the upper image reference frame, and p_1 represents the coordinates of the corresponding point expressed in the lower image reference frame. The scalar s is the scale factor, R is the two-dimensional rotation matrix previously defined, and $\mathrm{t}$is the translation vector accounting for the spatial offset between the two coordinate systems.

This equation therefore describes a two-dimensional similarity transformation, combining rotation, uniform scaling, and translation, and allows the mapping of the upper image onto the reference system of the lower image.

Accordingly, the similarity transformation establishes the geometric mapping between the two fields of view, allowing the velocity fields acquired by the two cameras to be expressed within a single, consistent reference system.

4. Warping and Image Fusion: The computed transformation was implemented in the form of a 3×3 homogeneous matrix and applied to the upper image through a warping operation, i.e., a geometric deformation that modifies its position, orientation, and scale according to the estimated similarity transformation.

At the same time, the lower image was projected into the same reference frame by applying the identity transformation, thus preserving its original geometry within the unified coordinate system.

Once both images were expressed in the same spatial domain, an image fusion procedure was performed. In the overlapping regions, the final pixel intensity was computed as the average of the corresponding intensity values from the two aligned images.

The result is a single coherent composite image that integrates the information acquired by both cameras, while preserving the characteristic lines as geometric references for alignment and ensuring continuity across the merged field of view.

5. Storage of Results: Finally, the following outputs were saved:

- The fused image resulting from the merging of the two acquisitions, ready for subsequent processing and visualization stages.
- The geometric transformation parameters (rotation, scale, and translation) in a separate file, allowing their reuse without the need to recompute the alignment and enabling the combined

statistical analysis of the velocity fields acquired by the two cameras.

Figure 19 below presents a representative example of the final merged result.

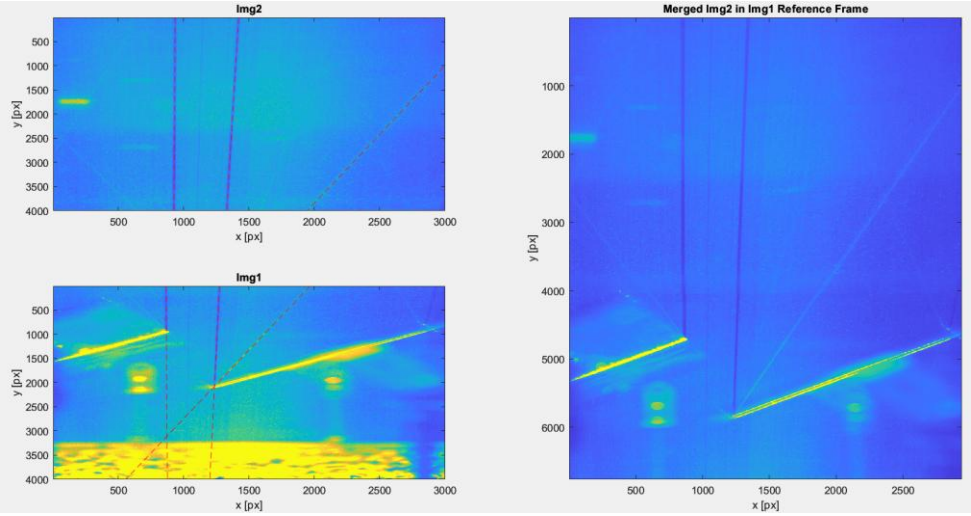

Figure 19: Merging procedure of the two camera views. The individual images (Img1 and Img2) are aligned using the light and shadow cones as reference lines and then combined into a single image in a common reference frame.

4.4 Description of the MATLAB code to compute the statistics

Once the geometric alignment of the reference systems was completed, the statistical characterization of the flow fields was performed.

To ensure that the entire procedure was organized, transparent, and fully reproducible, a configuration text file (README) was prepared. This file contains all relevant information associated with the different experimental tests performed.

For each test, the document specifies a unique naming convention, the adopted Δtvalues, the file containing the panel origin coordinates, and the image regions to be excluded or replaced during the analysis phase. In particular, the information concerning panel positioning and the identification of regions affected by blurring was obtained using

dedicated codes equipped with a graphical user interface (GUI). This interface enabled interactive definition of the panel geometry and selection of unreliable image regions. Once identified for each angular configuration, these elements were saved in dedicated folders and subsequently referenced within the configuration file.

The statistical computation was carried out using a script named test_mergert. At execution start, a configuration structure—referred to as metaraw—is defined. This structure collects all parameters required for processing, including:

- the path to raw data,
- the output directory,
- import options,
- and the selection between full-frame analysis or a subset of frames.

The metaraw structure is then passed to the various processing functions, ensuring centralized and consistent parameter management.

The script subsequently reads the README configuration file, which lists all experimental tests to be analysed along with their associated parameters, such as flow identifier, image time step Δt, reference elevations, and camera orientation. Each row of the file corresponds to an independent experimental test.

The core of the script consists of a loop iterating over the entire set of listed tests. For each test:

- The main parameters are extracted.
- The geometric transformation required to align the two PIV camera datasets is loaded.
- The velocity fields are merged into a unified reference frame.

Before performing any computation, the code checks whether a statistics file already exists for the current test. This avoids unnecessary recalculation and improves computational efficiency.

If statistics are not yet available, the script enters a second loop, analysing the test for different values of Δt.

For each Δt:

- The PIV fields from both cameras are loaded.
- The geometric transformation is applied.
- The velocity fields are fused.
- Descriptive temporal statistics are computed.

Specifically, the following quantities are evaluated:

- Statistical moments from first to fourth order,
- Turbulent kinetic energy (TKE),
- Vorticity.

After processing all Δt values, the results are saved in a dedicated file uniquely associated with the analysed test. The script then proceeds to the next test until all experimental cases have been processed.

The computed statistics are subsequently reprocessed to ensure coherent and uniform representation.

In this phase:

- All statistics files in the output directory are scanned.
- Files consistent with the adopted naming convention are selected.
- For each selected file, statistics computed at different Δtvalues are loaded and combined into a single representative mean field for the experimental test.

This operation is necessary to obtain a complete and consistent description of the flow field.

Given the characteristic evolution of the velocity profile in the analysed system, the use of two different Δt values significantly improve reconstruction quality:

- The larger Δt is better suited for velocity estimation in regions below the panels, where particle displacements are relatively small.
- The smaller Δt provides more accurate velocity estimation in regions above the panels, where stronger flow motions occur.

The combination of statistics obtained with different time steps therefore enables coherent representation of the entire flow domain.

During this phase, the test identifier is extracted from the file header, preserving the link between aggregated results and the corresponding experimental configuration. When specified by processing options, geometric information related to panel position and orientation, as well as excluded regions, is also loaded. These geometric data are appropriately converted and scaled to ensure consistency with the reference frame of the mean velocity field.

The integration of temporal statistics with geometric information ultimately produces a fully fused and consistent statistical field, representing the mean flow behaviour for each experimental test and constituting the primary output of this post-processing phase.

5. RESULTS ANALYSIS

5.1 Description of the plot obtained

Once the processing and post-processing phases of the experimental data were completed, the derived quantities were represented through two-dimensional contour maps to analyse their spatial distribution and their evolution under varying operating conditions.

To ensure clear, coherent, and directly comparable visualization, each statistical quantity was presented within a single figure including all analysed configurations. Specifically, each panel inclination was arranged along a dedicated row, within which the plots corresponding to the three tested discharge values were displayed side by side in increasing order from left to right. This layout enables direct observation of the effect of increasing discharge while maintaining a fixed geometric configuration.

The inclinations were ordered according to the sequence +20°, -20°, +35°, and -35°, allowing first a comparison between angles of equal magnitude but opposite sign, and subsequently an evaluation of the effect of increasing the inclination angle.

At the end of each row, a single colorbar common to the three plots of the same inclination was included. This choice ensures uniformity in the colour scale and enables direct comparison of the variable evolution as a function of discharge. Such an approach avoids interpretative ambiguities that could arise from differences in scale between adjacent plots.

Within each graph, the position of the inclined panel is explicitly indicated, providing immediate visual reference between the geometric configuration and the observed fluid dynamic phenomena.

Although the experimental channel has a total height of 0.50 m, only the lower portion of the domain (up to $y = 0.20$ m) was represented in the contour maps. This decision was made to emphasize the region near the panel, where fluid–structure interaction is concentrated and where velocity gradients and inclination-induced variations are most pronounced. The upper portion of the channel, while physically present, is not critical for the local analysis addressed in this study.

The following sections analyse the main statistical quantities obtained from the PIV processing, namely:

- Mean horizontal velocity U_m,
- Mean vertical velocity V_m,
- Streamlines,
- Turbulent kinetic energy (TKE),
- Vorticity,
- Reynolds stresses.

Each of these quantities characterizes a specific aspect of flow dynamics, respectively related to momentum distribution, vertical flow deviation, global flow structure, turbulence intensity, local rotational behaviour, and turbulent momentum transport mechanisms.

Mean horizontal velocity U_m

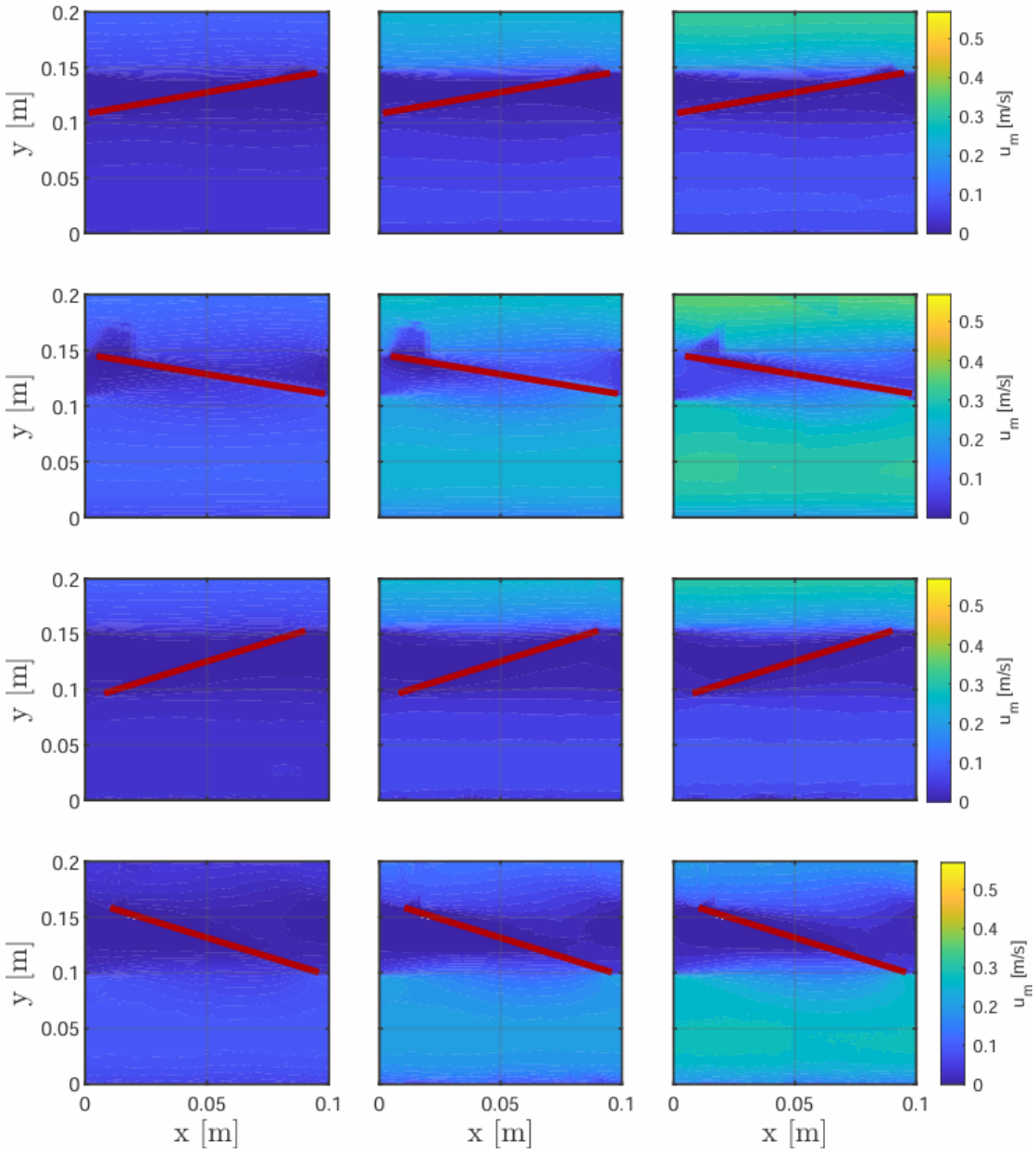

Figure 20: Colormap of the mean horizontal velocity field U_m within the measurement domain for the different panel inclinations and flow rates analysed. The columns represent increasing flow rates (35, 75, and 95 L/s from left to right), while the rows correspond to the panel inclinations (+20°, −20°, +35°, −35° from top to bottom). The colormap, common to all subplots, shows velocity values expressed in m/s. The red line indicates the position of the inclined panel inside the channel.

The analysis of the mean horizontal velocity fields U_m allows a detailed description of momentum distribution within the channel and an assessment of the combined influence of discharge and panel inclination. In all configurations, a typical vertical profile of open-

channel flow is observed, with higher velocity values at greater elevations and a progressive reduction toward the bottom, consistent with viscous friction effects at the channel bed.

As discharge increases, a general amplification of velocity levels is observed throughout the domain. The intensification of high-velocity regions highlights how increased discharge enhances the available momentum without substantially altering the global structure of the flow field. The acceleration and deceleration regions induced by the panel remain spatially located in the same areas, becoming simply more pronounced at higher flow rates. Therefore, discharge can be interpreted as exerting primarily a scaling effect, amplifying pre-existing flow features without modifying their qualitative nature.

Panel inclination, on the other hand, represents the dominant parameter influencing the reorganization of the velocity field. In the case of positive inclination (+20° and +35°), with the panel oriented upstream, the flow encounters a surface that partially opposes the main flow direction. This configuration induces a redistribution of momentum toward the upper portion of the domain. A localized acceleration is observed near the downstream edge of the panel, while a slight reduction in velocity occurs beneath it. The effect becomes more pronounced at +35°, where the increased inclination enhances flow obstruction and produces stronger longitudinal gradients. Consequently, the vertical velocity profile appears more distorted compared to the +20° case, with a more marked concentration of velocity in the upper region of the analysed domain.

In contrast, for negative inclinations (-20° and -35°), where the panel is oriented downstream, the flow behaviour changes significantly. The inclined surface aligns more favourably with the main flow direction,

allowing the fluid to slide along the panel with reduced frontal opposition. However, a different momentum redistribution pattern emerges. In fact, momentum tends to concentrate more in the lower portion of the domain, while the upper region exhibits an extended area of relatively reduced velocity. The vertical profile thus assumes a more asymmetric configuration, with a clear downward shift of the high-velocity region. As in the positive cases, the effect is amplified at -35°, where the geometric deviation imposed by the panel is stronger and the reorganization of the mean field more evident.

Overall, the analysis of U_m fields demonstrates that panel inclination is the dominant factor governing the modification of momentum distribution within the channel, whereas discharge primarily intensifies velocity magnitudes without altering the qualitative flow configuration. Upstream-oriented inclinations tend to concentrate velocity near the free surface, while downstream-oriented inclinations promote redistribution toward the lower region of the domain, producing more asymmetric vertical profiles.

Mean vertical velocity V_m

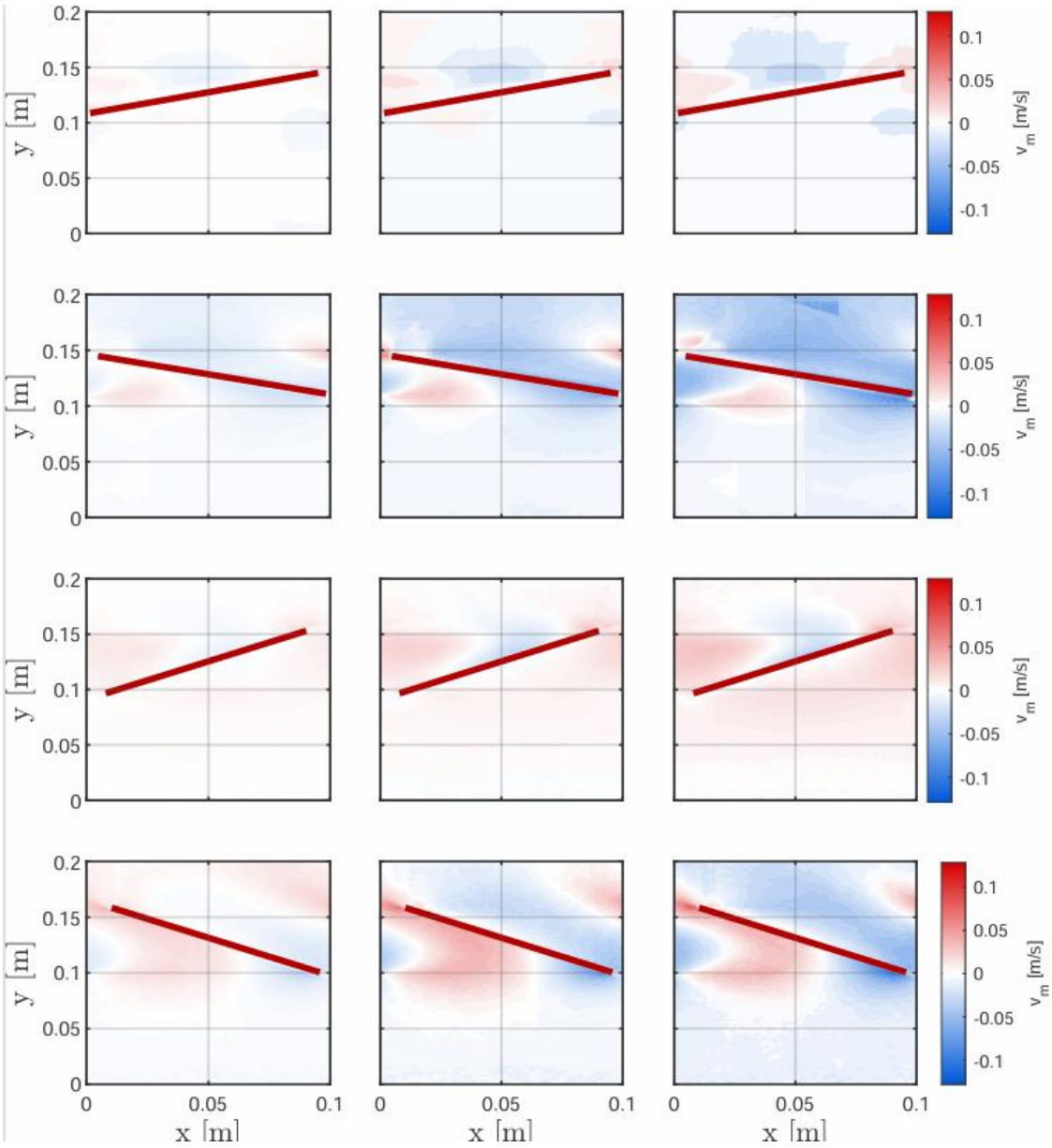

Figure 21: Colormap of the mean vertical velocity field V_m within the measurement domain for the different panel inclinations and flow rates analyzed. The columns represent increasing flow rates (35, 75, and 95 L/s from left to right), while the rows correspond to the panel inclinations (+20°, −20°, +35°, −35° from top to bottom). The colormap, common to all subplots, shows velocity values expressed in m/s. The red line indicates the position of the inclined panel inside the channel.

The vertical velocity component highlights the influence of panel inclination on the reorganization of the flow within the channel. The use of a diverging colormap centered at zero allows a clear identification of

upward motion (red) and downward motion (blue), while white regions indicate areas where the vertical component is negligible.

For the +20° inclination, the field appears relatively weak and uniform. Variations in $v_m$are limited and mainly confined to the vicinity of the panel, where the flow undergoes slight vertical deviations due to the inclined surface. Increasing the discharge leads to higher velocity magnitudes, but the overall structure of the field remains substantially unchanged, without the development of extended regions of strong vertical motion or large-scale recirculation.

When the inclination is increased to +35°, the flow behaviour changes significantly. A more pronounced alternation between upward and downward motion develops along the panel surface, indicating stronger vertical gradients and a more marked deflection of the main flow. As the discharge increases, these regions intensify both in magnitude and spatial extent, suggesting enhanced shear effects and a stronger interaction between the incoming flow and the inclined panel.

In the case of -35° inclination, the vertical velocity distribution differs substantially from the positive-angle configurations. The panel orientation induces a deflection of the flow in the opposite direction, resulting in extended regions where the vertical component maintains a coherent sign along the inclined surface. The increase in discharge amplifies this behaviour, making the redistribution of the mean flow more evident and structured.

For the -20° configuration, the field exhibits a clearly organized pattern, with alternating regions of upward and downward motion concentrated near the panel. This behaviour reflects the presence of strong vertical gradients and a significant redistribution of momentum induced by the inclined surface. As the discharge increases, these structures become

more intense and better defined, indicating a progressively stronger interaction between the main flow and the panel.

Overall, the analysis of the vertical velocity field confirms that panel inclination is the dominant parameter controlling flow deflection and vertical momentum redistribution. The discharge primarily acts as an amplification factor, increasing the magnitude of the observed phenomena, while the geometric configuration governs the spatial structure and organization of the upward and downward motion regions.

Streamlines

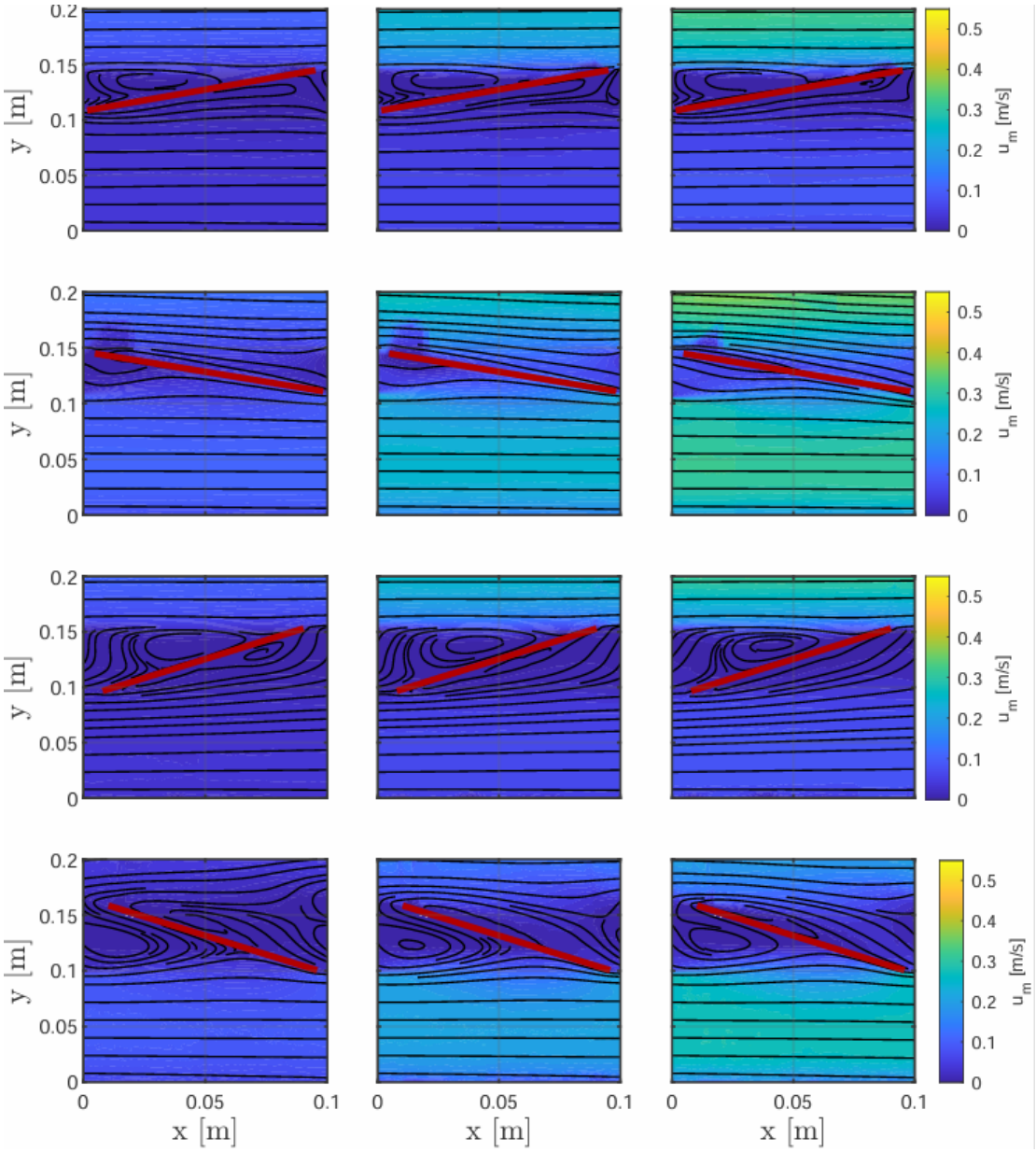

Figure 22: Streamlines of the mean velocity field for the analysed panel inclinations and flow rates. Columns correspond to increasing discharge (35, 75, and 95 L/s from left to right), whereas rows represent the angular configurations (+20°, −20°, +35°, −35°). The red line marks the panel location within the channel.

Streamlines provide a clear visualization of the global flow structure and allow identification of marked deviations or recirculation regions generated by the interaction between the flow and the inclined panel. In all configurations, the flow remains undisturbed in regions sufficiently far from the panel. Near the panel, however, the streamlines undergo a

noticeable deviation, adapting to the geometry imposed by the inclined surface. For positive inclination angles, the flow tends to rise along the panel, following its slope and concentrating in the upper portion of the domain. For the larger angle (+35°), the streamlines appear more strongly curved and a closed-flow region becomes visible above the panel, indicating the formation of a localized vortical structure. This phenomenon is less pronounced in the +20° case, where the deviation is more gradual and no extended recirculation regions are observed.

For negative inclination angles, the flow behaviour exhibits more evident differences. The streamlines bend more significantly within the central region of the domain, and more extended closed structures are observed compared to the positive cases. For -35°, a well-developed vortical region appears, with streamlines describing clearly defined circular trajectories. This suggests stronger flow separation and enhanced local instability induced by the interaction with the panel.

Increasing the discharge does not qualitatively alter the streamline structure, but it makes the curvature of the trajectories more evident, and any recirculation regions more clearly defined. The observed structures maintain the same spatial location as discharge varies, confirming that geometry is the dominant parameter governing the global flow configuration. Overall, the streamline analysis highlights that panel inclination does not merely modify the local velocity distribution but can significantly reorganize the overall flow structure, leading to the formation of vortical regions of varying extent depending on the inclination angle. Configurations with larger inclination angles exhibit stronger flow–structure interaction and a greater tendency toward closed-flow formation, indicative of a more complex and less uniformly developed velocity field.

Turbulent kinetic energy (TKE)

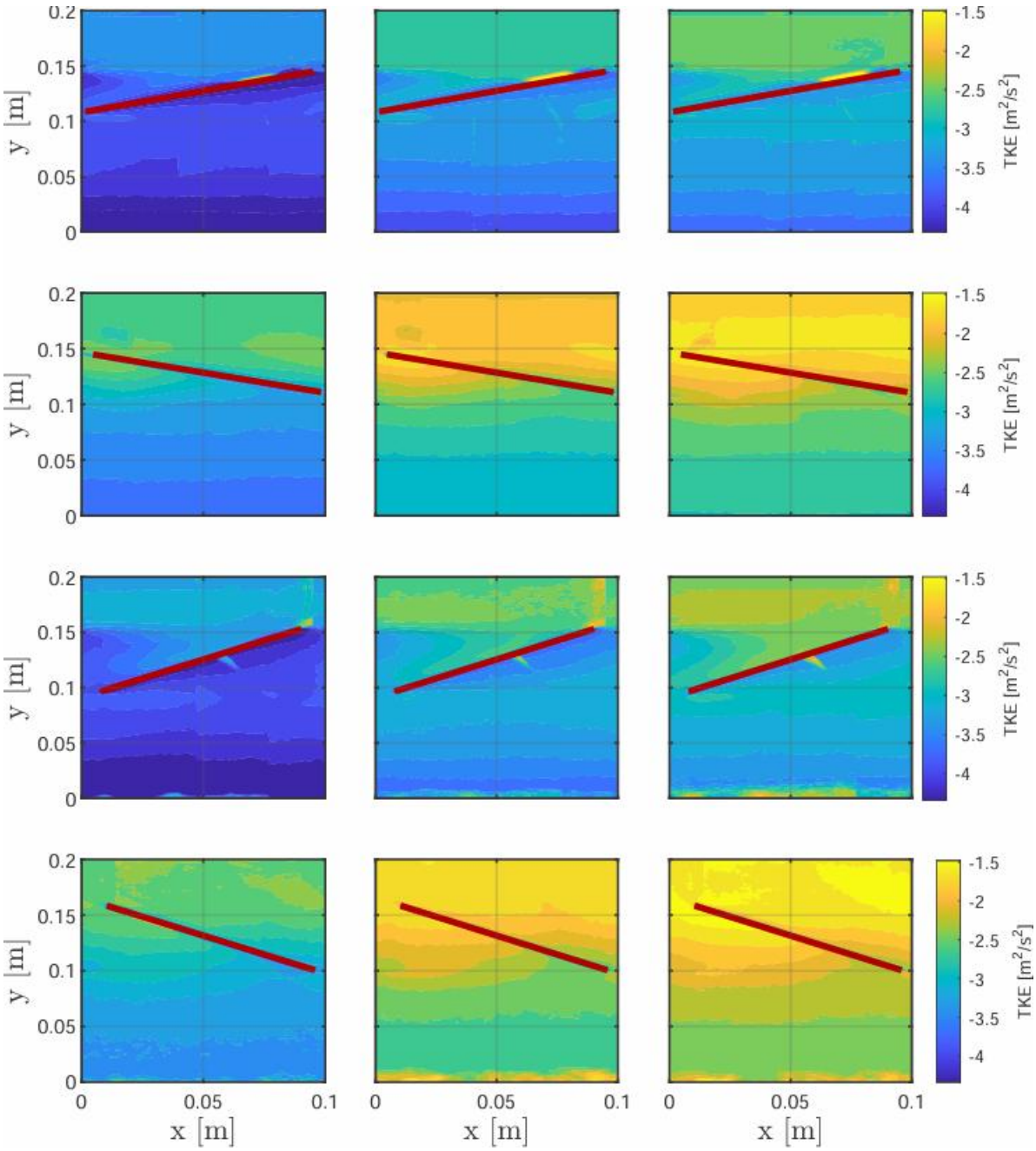

Figure 23: Colormap of the turbulent kinetic energy k displayed on a logarithmic scale (base 10) for the analyzed panel inclinations and flow rates. Columns correspond to increasing discharge (35, 75, and 95 L/s from left to right), while rows represent the angular configurations (+20°, −20°, +35°, −35°). The logarithmic color scale is uniform across all subplots. The red line indicates the position of the inclined panel.

The turbulent kinetic energy (TKE) maps clearly highlight the regions where the interaction between the flow and the panel generates intensified velocity fluctuations. Unlike mean quantities, TKE does not

describe the distribution of momentum but rather identifies zones of turbulent production associated with strong velocity gradients and potential flow separation phenomena.

In all configurations, the highest TKE values are concentrated in the upper portion of the analysed domain, particularly near the panel. Away from the inclined element—and especially toward the channel bed—TKE levels are significantly lower, indicating a more ordered and less perturbed flow regime.

As discharge increases, a general rise in TKE levels is observed, accompanied by a progressive expansion of high-intensity turbulent regions. This behaviour is consistent with the increased velocity gradients observed in the mean flow fields: the greater the available momentum, the stronger the turbulent energy production. However, the spatial location of the high-TKE regions remains essentially unchanged as discharge varies, confirming that geometry is the dominant factor governing the localization of turbulence generation.

The most significant differences emerge as the inclination angle changes. For +20°, a relatively confined region of elevated TKE is observed along the panel and near its upper edge. When the inclination increases to +35°, this region expands and the peak values increase, indicating more intense turbulent production and a wider affected area. This suggests that larger positive inclinations enhance velocity gradients along the panel, promoting the formation of a more energetic shear layer.

For -20°, the TKE distribution appears more diffuse within the central region of the domain, with elevated values extending downstream of the panel. The effect is further amplified at -35°, where the high-TKE area expands significantly and involves a larger portion of the upper domain.

In this configuration, turbulent production is more pronounced and less localized, consistent with the stronger flow reorganization observed in the streamline analysis.

Overall, the TKE analysis demonstrates that increasing panel inclination intensifies turbulence production and broadens its spatial distribution. Configurations with larger angles exhibit stronger flow–structure interaction, leading to the formation of high-turbulence regions in the upper part of the domain. TKE therefore confirms that geometry-induced modifications are not limited to mean flow redistribution but also result in increased instability and greater flow complexity.

Vorticity

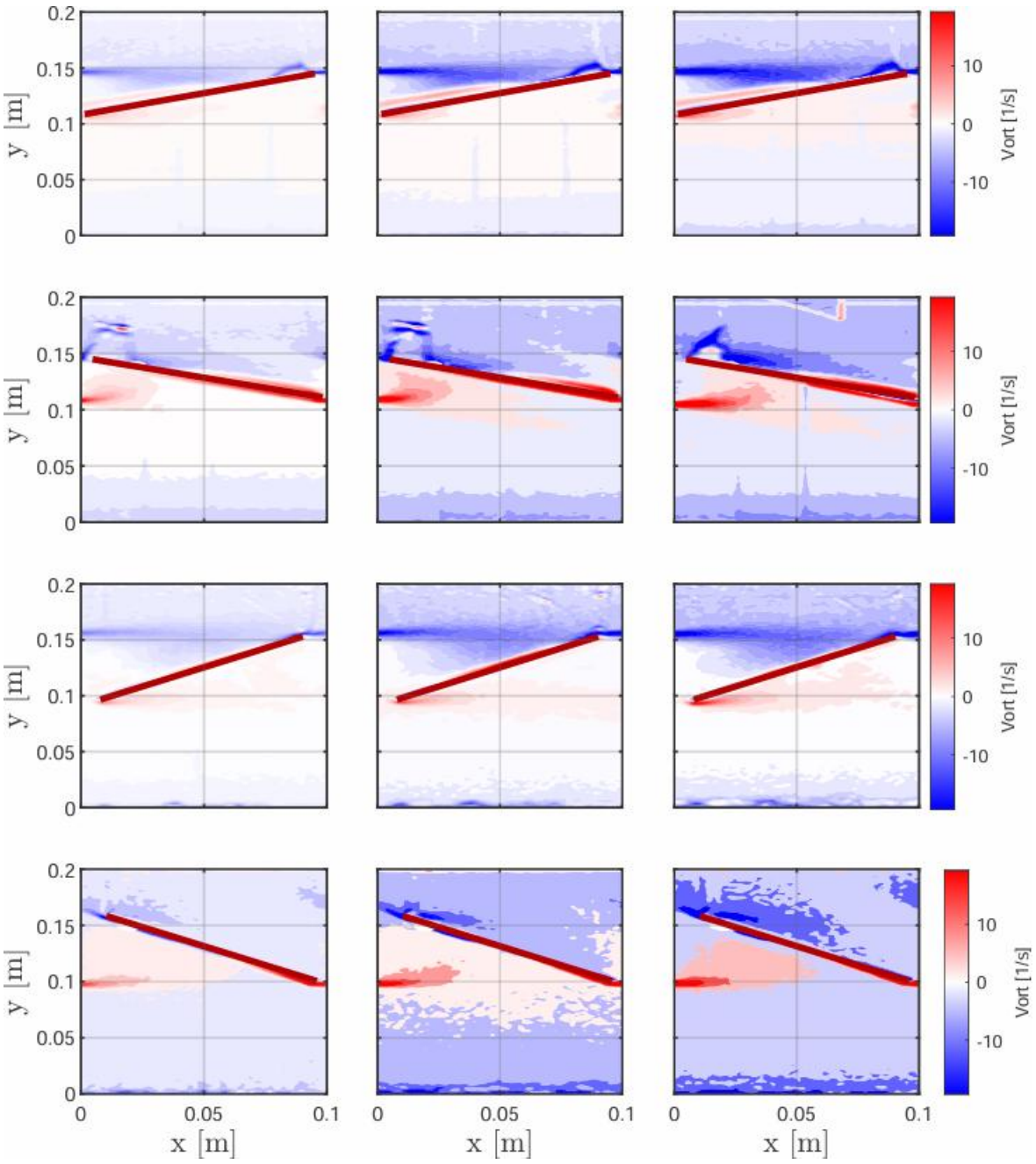

Figure 24: Colormap of the spanwise vorticity field ω_z for the different panel inclinations and flow rates considered. The columns represent increasing discharge (35, 75, and 95 L/s from left to right), while the rows correspond to the panel inclinations (+20°, −20°, +35°, −35°). The color scale, common to all subplots, shows vorticity values expressed in 1/s. The red line marks the location of the inclined panel.

The vorticity maps highlight the regions where the velocity field exhibits strong transverse gradients, thereby identifying localized rotational structures. Far from the panel, vorticity values remain close to zero

across most of the analysed domain, indicating a predominantly irrotational flow in areas not directly influenced by the obstacle. The most significant variations are instead concentrated along the panel and in its immediate vicinity.

In all configurations, shear layers of opposite sign develop along the two sides of the panel, indicating the presence of pronounced velocity gradients generated by the interaction between the main flow and the inclined surface. These shear layers extend along the panel length and intensify toward the downstream edge, where the flow undergoes more evident reorganization.

An increase in discharge results in higher vorticity magnitudes, making regions of both positive and negative values more pronounced. However, the spatial location of the shear layers remains unchanged, confirming that geometry governs the positioning of rotational structures, while discharge primarily amplifies their intensity.

For +20°, the vorticity distribution remains confined along the panel, with a well-defined but spatially limited shear layer. When the inclination increases to +35°, the shear layer becomes stronger and rotational regions extend further into the upper portion of the domain, consistent with the enhanced flow deviation observed in previous analyses.

In the -20° configuration, the vorticity structure appears more diffuse, with alternating-sign regions extending more prominently into the central part of the domain. For -35°, this effect becomes even more evident: shear layers are more intense, and a broader area exhibits significant vorticity values, indicating stronger local instability and a more complex reorganization of the flow field.

Overall, the vorticity analysis confirms that increasing panel inclination enhances velocity gradients along the panel, generating stronger shear

layers and more developed rotational structures. Configurations with larger inclination angles therefore exhibit more energetic flow–structure interaction and increased local instability. Vorticity thus provides a direct measure of the dynamic complexity introduced by the geometry, complementing the insights derived from the mean and turbulent flow analyses.

Reynolds stresses

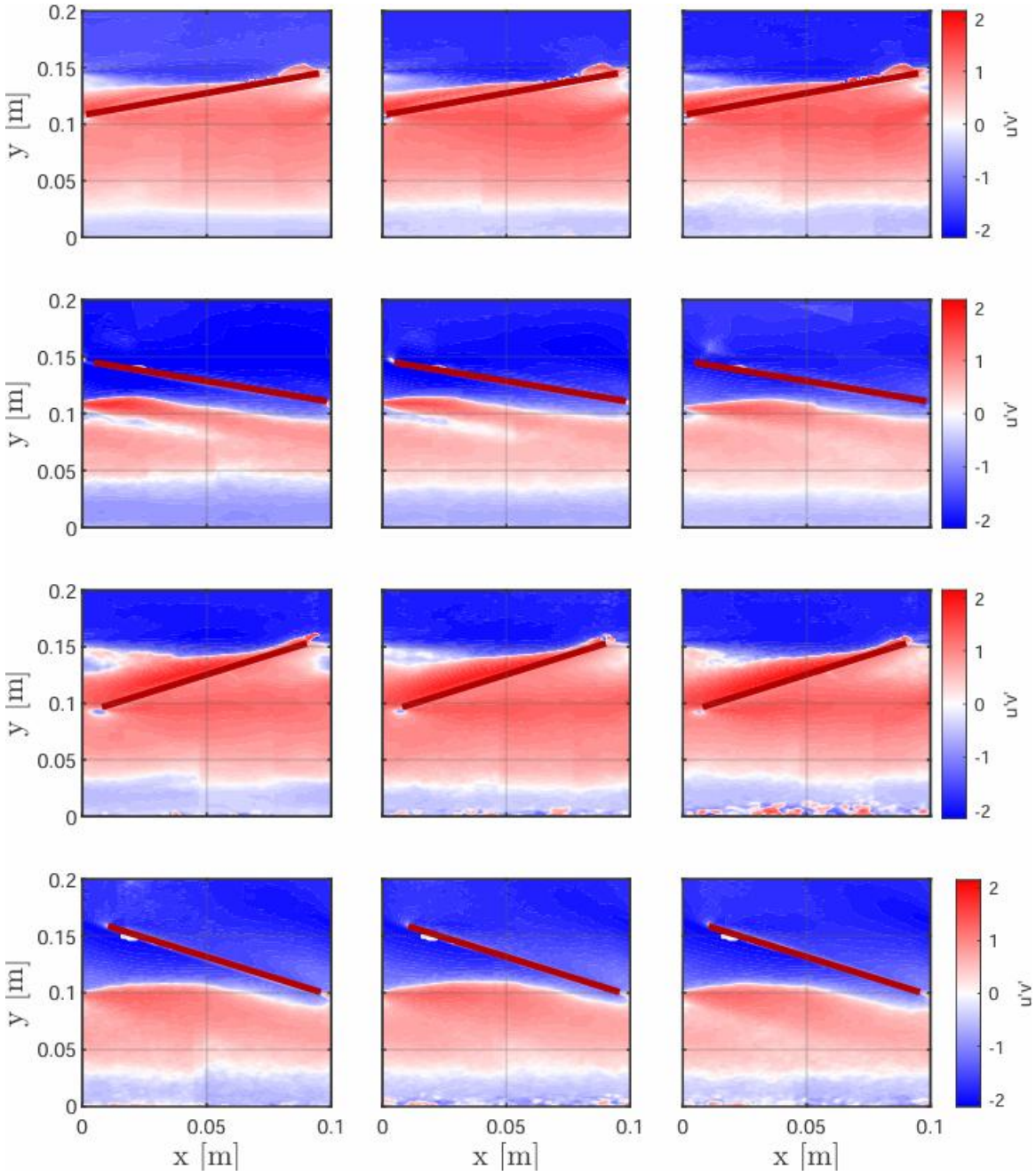

Figure 25: Colormap of the Reynolds shear stress $u'v'$ within the measurement domain for the investigated panel inclinations and flow rates. Columns show increasing discharge (35, 75, and 95 L/s from left to right), while rows correspond to the angular configurations (+20°, −20°, +35°, −35°). The color scale, uniform across all subplots. The red line indicates the panel position inside the channel.

The Reynolds stress fields $u'v'$ provide insight into the turbulent transport of momentum between the longitudinal and vertical directions. Unlike TKE, which quantifies the overall intensity of velocity fluctuations, the

term $u'v'$ directly reflects the efficiency with which these fluctuations contribute to turbulent momentum transfer within the flow field.

In all configurations, a clear vertical stratification of the domain is observed: the upper region is predominantly characterized by negative values, while the central-lower portion exhibits positive values. This distribution reflects the presence of a shear layer near the panel, where strong velocity gradients generate intense turbulent exchange.

Increasing discharge leads to higher magnitudes of $u'v'$, enhancing the contrast between regions of opposite sign. However, the overall structure of the field remains unchanged, once again confirming that discharge amplifies existing mechanisms without altering their spatial configuration.

The most evident differences arise with changes in inclination angle.

For +20°, the Reynolds stress field appears relatively regular, with a localized region of maximum turbulent exchange along the panel and near its upper edge. When the inclination increases to +35°, this region intensifies and expands, indicating stronger vertical velocity gradients and enhanced turbulent production associated with the shear layer.

In the -20° configuration, the distribution of $u'v'$ appears more extended within the central portion of the domain, with a broader positive region and a more developed negative region above. For -35°, the effect becomes even more pronounced: the zone of maximum turbulent stress expands significantly, involving a larger portion of the domain and indicating more intense and spatially distributed momentum transfer.

Overall, the $u'v'$ fields confirm that panel inclination influences not only turbulence intensity but also the way momentum is vertically redistributed. Larger inclination angles generate a stronger shear layer and more significant turbulent transfer, consistent with the trends

observed in the TKE and vorticity maps. The Reynolds stresses thus provide a quantitative representation of the turbulent exchange processes induced by geometry-driven velocity gradients.

5.2 Comparison with the numerical model results

To assess the capability of the numerical model to reproduce the experimentally observed phenomena, a direct comparison was performed between the flow fields obtained through Particle Image Velocimetry (PIV) and those derived from the solution of the Reynolds-Averaged Navier–Stokes equations (RANS).

The analysis was conducted for a discharge of 95 L/s, considering the two panel inclination configurations of +20° and +35°, to investigate the effect of increasing the angle under identical operating conditions.

For each configuration, the experimental results are shown on the left-hand side of the figures, while the corresponding numerical fields are displayed on the right-hand side. This layout enables an immediate visual comparison between the two representations, facilitating the identification of similarities and discrepancies in the spatial distribution of the analysed quantities. The comparison was carried out under identical geometric and operating conditions for both experiment and simulation, ensuring consistency between the two approaches and allowing a meaningful evaluation of the predictive capability of the numerical model.

The comparative analysis follows the same sequence adopted in the discussion of the experimental results, thereby maintaining coherence and physical continuity in the interpretation of the flow phenomena. Specifically, the comparison begins with the mean horizontal velocity field U_m, proceeds to the mean vertical velocity V_m and the streamline

analysis, and subsequently examines the turbulent quantities, namely turbulent kinetic energy (TKE) and vorticity.

This structured progression—from mean flow description to characterization of flow structure and turbulence production mechanisms—provides a comprehensive assessment of the numerical model performance relative to the experimental data.

Mean horizontal velocity U_m

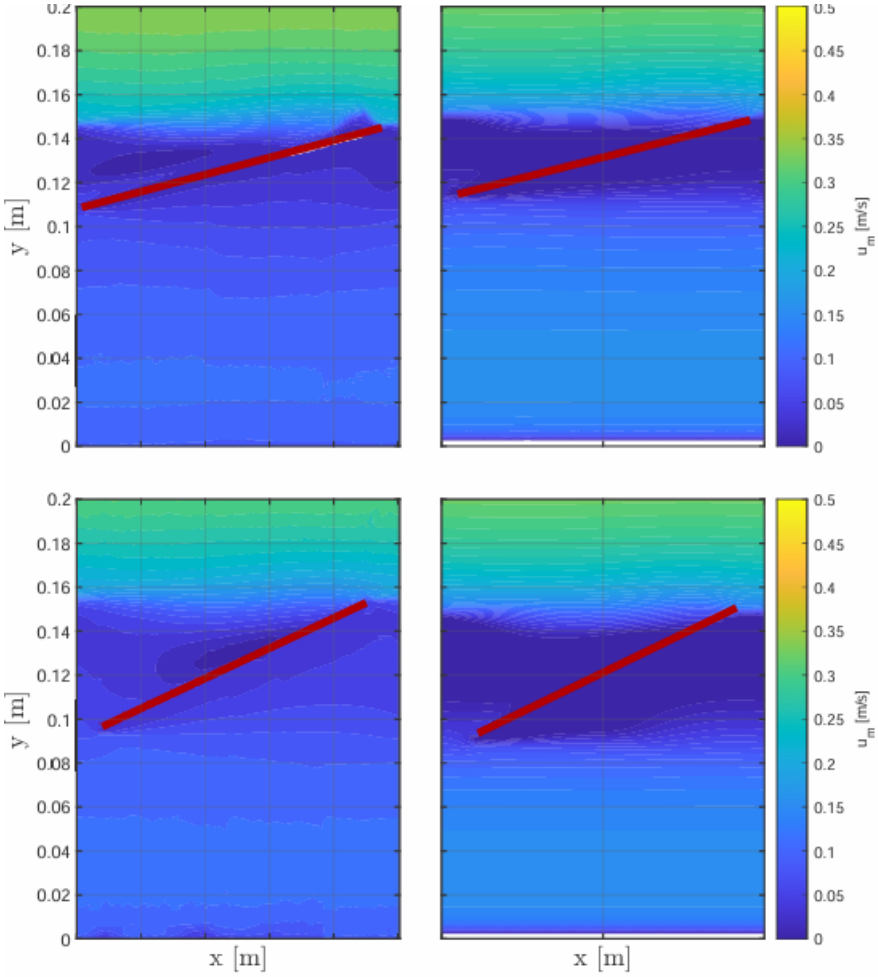

Figure 26: Colormap of the mean horizontal velocity field U_m for two panel inclinations at a flow rate of 95 L/s. The left column reports experimental results obtained by PIV, while the right column shows the corresponding RANS numerical simulations. The top row refers to the +20° configuration, while the bottom row corresponds to the +35° configuration. The colormap represents velocity values expressed in m/s and is uniform within each experimental–numerical pair. The red line indicates the position of the inclined panel inside the channel.

The comparison of the mean horizontal velocity fields shows good qualitative agreement between experimental and numerical results for both considered inclinations.

For the +20° configuration, the numerical model correctly reproduces the vertical velocity distribution, exhibiting a progressive increase toward the free surface and a reduction near the channel bed. The reorganization of the flow field in the vicinity of the panel is also consistent with experimental observations, particularly regarding the location of the strongest gradient along the inclined surface. However, the numerical field appears smoother and more continuous than the experimental one, which displays greater local variability and minor non-uniformities inherent to the statistical nature of Particle Image Velocimetry measurements. Near the upper edge of the panel, the numerical result shows a slight attenuation of the gradient, leading to a smoother transition between regions of different velocity.

In the +35° case, the interaction between the flow and the panel becomes more intense, resulting in a stronger vertical gradient along the inclined surface. The numerical model again captures the general behaviour of the field, correctly reproducing the redistribution of velocity within the upper portion of the domain. Nevertheless, compared to the experimental data, the numerical field exhibits lower intensity in the local variations near the panel, suggesting a potential underestimation of the highest gradients. This discrepancy is particularly noticeable in the region immediately above the panel, where the experimental field displays a sharper variation than the numerical representation.

Overall, for both inclinations at 95 L/s, the Reynolds-Averaged Navier–Stokes equations (RANS) model demonstrates good capability in reproducing the mean flow structure and the global momentum

distribution. The observed discrepancies are primarily related to the smoother nature of the numerical field and to the inherent damping of local gradients introduced by turbulence modelling. The comparison of U_m therefore indicates satisfactory qualitative agreement, with differences confined to regions characterized by stronger velocity gradients.

Mean vertical velocity V_m

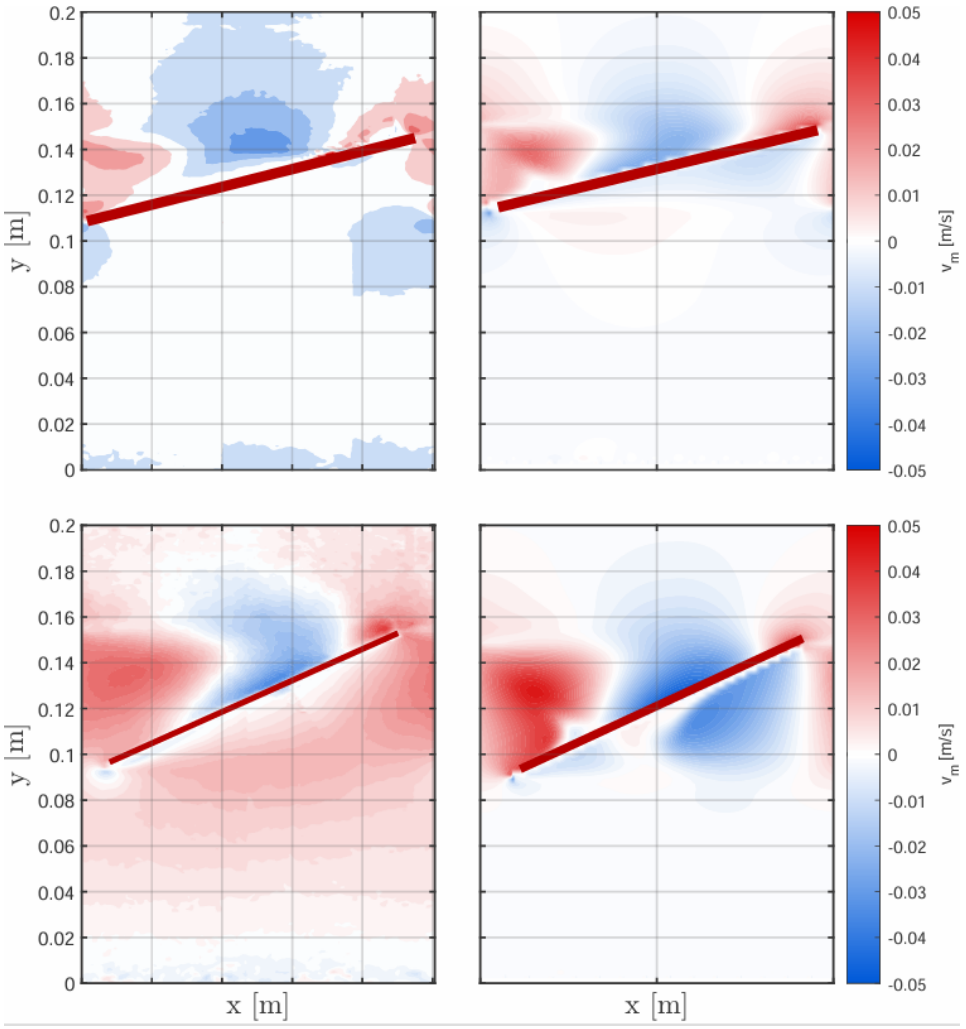

Figure 27: Colormap of the mean vertical velocity field V_m for two panel inclinations at a flow rate of 95 L/s. Experimental PIV results are shown in the left column, while RANS numerical simulations are reported in the right column. The top row refers to the +20° configuration, while the bottom row corresponds to the +35° configuration. The colormap represents velocity values expressed in m/s. The red line indicates the position of the inclined panel within the channel.

The comparison of the mean vertical velocity component reveals more pronounced differences than those observed for the streamwise velocity, as $V_m$is smaller in magnitude and therefore more sensitive to local gradients and panel-induced flow deviations.

For the +20° configuration, the experimental field is characterized by generally low $V_m$values across most of the domain, with a localized region of deviation developing in proximity to the panel. A weak upward motion appears near the trailing portion of the panel, while a broader region of downward motion is observed in the upper part of the domain. The numerical model qualitatively reproduces the presence and approximate location of these features; however, the distribution appears more regular and spatially organized. In particular, the numerical solution exhibits smoother and more coherent structures, whereas the experimental field shows a slightly more diffuse pattern, likely reflecting measurement variability and local flow fluctuations captured by the PIV technique.

In the +35° case, the vertical deviation becomes significantly more intense and structured. The experimental field displays a pronounced alternation between positive and negative regions along and above the panel, indicating a stronger deflection of the main flow and a more complex redistribution of vertical momentum. The numerical model captures the presence of these opposite-sign regions and correctly predicts their spatial location relative to the panel. Nevertheless, the computed field appears more symmetric and spatially concentrated, while the experimental results exhibit a broader and more irregular deviation pattern. This difference suggests that the Reynolds-Averaged Navier–Stokes formulation, by its time-averaged nature, tends to emphasize spatial coherence and smooth gradients, whereas the

experimental measurements retain the effects of local variability and small-scale flow structures.

Overall, the analysis of V_m confirms that the numerical model successfully reproduces the location and general characteristics of the panel-induced vertical flow deviation. However, it tends to represent the vertical structures in a more organized and less irregular manner than observed experimentally. The discrepancies are particularly evident in regions of strong vertical gradients, where the relatively small magnitude of the vertical component makes it more sensitive to modelling assumptions and experimental uncertainties.

Streamlines

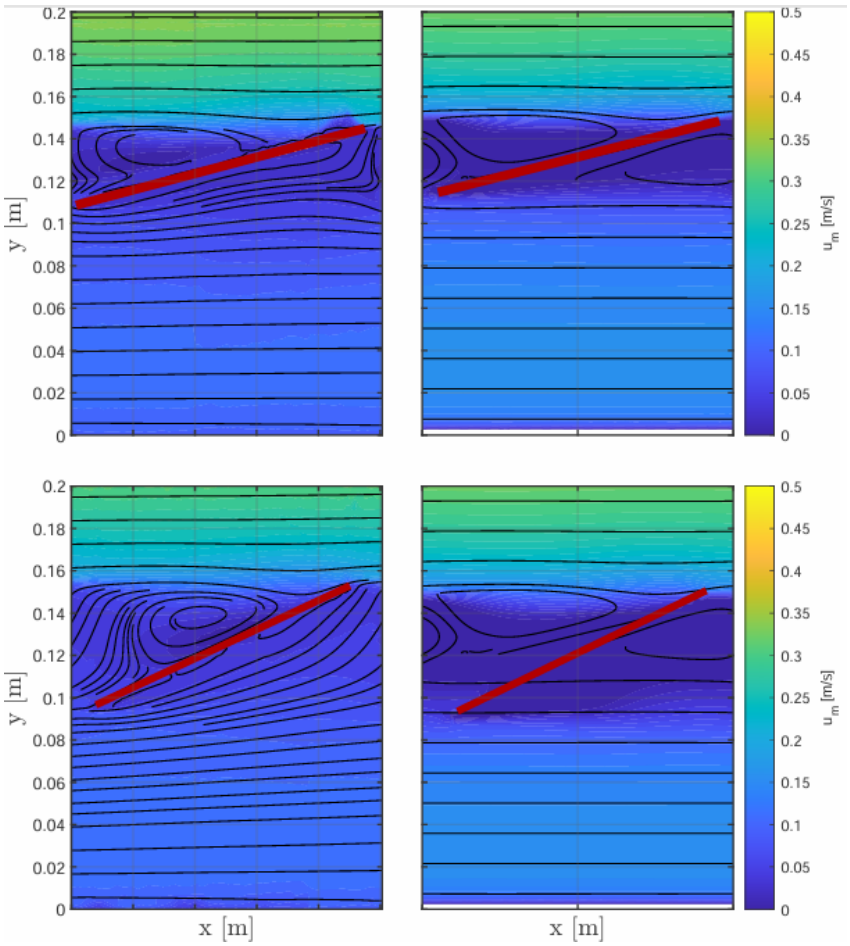

Figure 28: Streamlines of the mean velocity field for the +20° and +35° configurations at 95 L/s. Experimental results are shown in the left column and numerical simulations in the right column. The top row refers to the +20° configuration, while the bottom row corresponds to the +35° configuration. The red line marks the inclined panel location.

The streamline analysis allows assessment of the numerical model's capability to reproduce the global flow structure, and particularly the potential formation of recirculation regions near the panel.

For the +20° inclination, the experimental field clearly shows a deviation of the streamlines in the upper portion of the domain, with the formation of a closed-flow region immediately above the panel. This vortical structure is well developed and occupies a significant portion of the region close to the free surface. In the corresponding numerical result, the deviation of the streamlines is correctly reproduced, and the presence of a recirculation region is recognizable. However, the structure appears more regular, less extended, and characterized by sharper contours compared to the experimental case. The model therefore captures the phenomenon but provides a smoother and less complex representation.

In the +35° configuration, the interaction between the flow and the panel becomes more intense, resulting in a more pronounced reorganization of the streamlines in the experimental field. A larger and well-defined vortical structure is observed, with strongly curved trajectories indicating clearer flow separation. The numerical model qualitatively reproduces the presence of the recirculation region, but with smaller spatial extension and reduced curvature of the streamlines compared to the experimental data. The vortical structure appears more compact and less vertically developed.

In both configurations, far from the panel, the streamlines remain essentially parallel to the longitudinal axis of the channel in both experimental and numerical fields, indicating good agreement in the description of the undisturbed flow. The discrepancies are therefore primarily concentrated in the fluid–structure interaction region, where

the Reynolds-Averaged Navier–Stokes equations (RANS) model tends to represent vortical structures in a more regular and less spatially extended manner than observed experimentally.

Overall, the comparison of streamlines shows that the numerical model successfully captures the presence and location of the main recirculation structures generated by the panel but tends to underestimate their spatial extent and structural complexity, particularly for the larger inclination angle.

Turbulent kinetic energy (TKE)

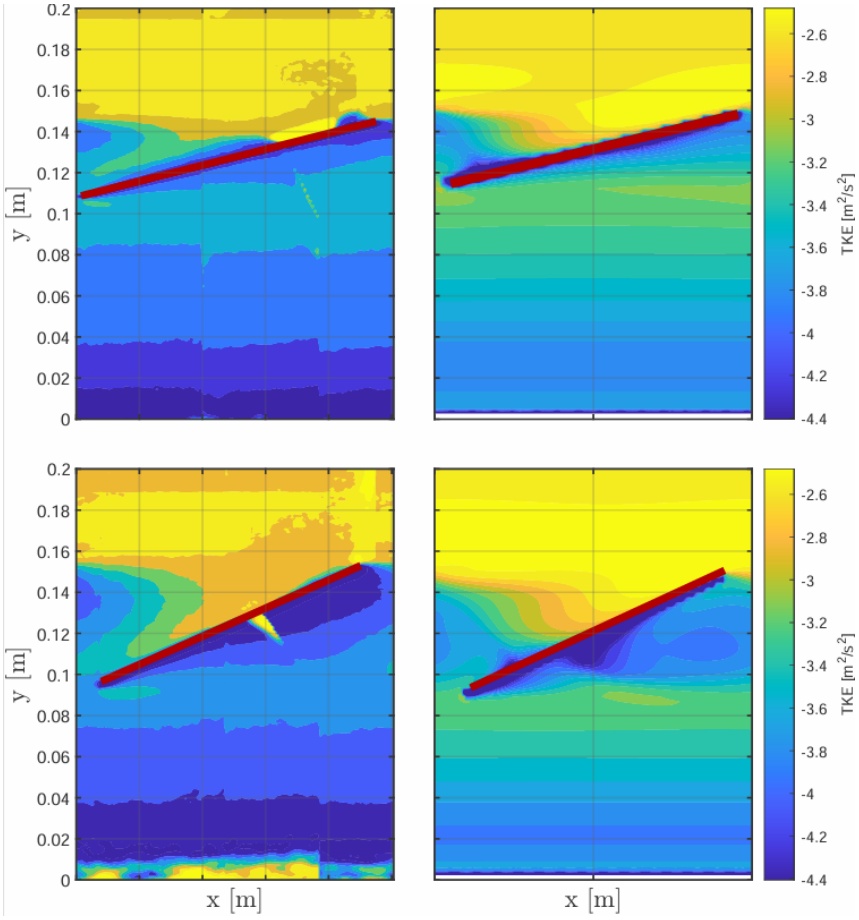

Figure 29: Colormap of the turbulent kinetic energy kdisplayed on a logarithmic scale (base 10) for the +20° and +35° configurations at a flow rate of 95 L/s. Experimental results (PIV) are shown in the left column and numerical simulations (RANS) in the right column. The top row refers to the +20° configuration, while the bottom row corresponds to the +35° configuration. The logarithmic colour scale represents k values in m^2/s^2. The red line indicates the panel position.

The comparison of the turbulent kinetic energy (TKE) fields highlights more pronounced differences than those observed for the mean quantities, since TKE is directly linked to turbulence modelling and is therefore more sensitive to the approximations introduced by the Reynolds-Averaged Navier–Stokes equations (RANS) approach.

For the +20° inclination, the experimental field shows a region of elevated TKE localized along the panel and near its upper edge, where velocity gradients are strongest. The numerical model reproduces the presence of this region, but the distribution appears more uniform and progressively varying. In particular, the transition between regions of different turbulence intensity is more gradual in the numerical field, whereas the experimental data exhibit sharper variations and greater spatial irregularity.

In the +35° case, the interaction between the flow and the panel becomes more energetic, resulting in a broader region of high TKE in the experimental field, extending into the upper portion of the domain. The numerical model correctly identifies the area of increased turbulence production near the panel; however, it tends to represent it with a smaller spatial extent and a smoother distribution. The high-TKE region appears more concentrated and less diffuse than in the experimental results, suggesting an underestimation of turbulent diffusion or attenuation of local peaks.

In both configurations, away from the panel, the numerical model yields a more regular and vertically stratified TKE distribution, whereas the experimental field shows greater variability, particularly near the free surface and the channel bed. This difference is consistent with the time-averaged nature of the RANS solution, which filters out smaller-scale fluctuations and produces a more uniform turbulent field.

Overall, the TKE comparison indicates that the numerical model can correctly identify the main regions of turbulence production and reproduce their spatial location, but it tends to smooth the strongest gradients and reduce the spatial extent of high-energy regions, especially at the larger inclination angle. The discrepancies are therefore most evident in the zones of strong fluid–structure interaction, where the experimental flow exhibits greater complexity.

Vorticity

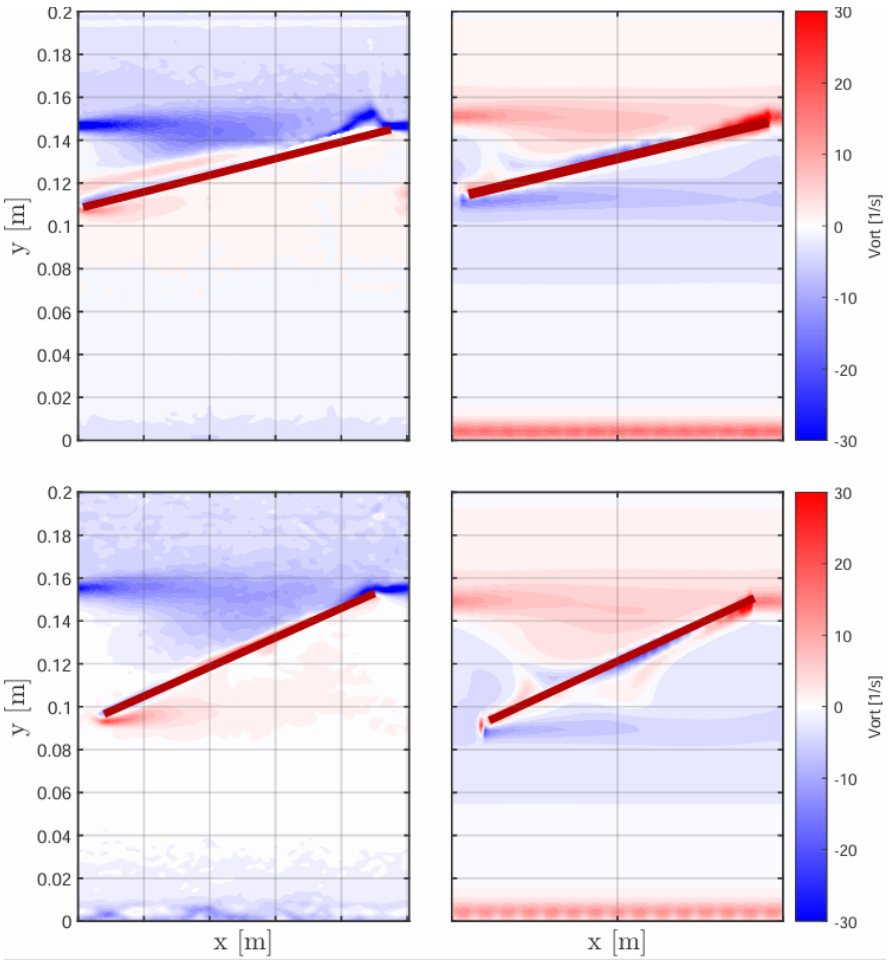

Figure 30: Colormap of the spanwise vorticity field ω_z for two panel inclinations at 95 L/s. The left column reports experimental PIV data, while the right column presents RANS numerical results. The top row refers to the +20° configuration, while the bottom row corresponds to the +35° configuration. The colour scale shows vorticity values expressed in 1/s. The red line marks the location of the inclined panel.

The comparison of the vorticity fields provides insight into the numerical model's ability to reproduce the shear layers and rotational structures generated by the interaction between the flow and the panel. Since vorticity is directly related to transverse velocity gradients, it is particularly sensitive both to experimental resolution and to the approximations introduced by the Reynolds-Averaged Navier–Stokes equations (RANS) modelling approach.

For the +20° inclination, the experimental field highlights a well-defined shear layer developing along the panel, with a clear alternation of sign near its upper edge. The distribution appears relatively thin and localized, with intense variations concentrated along the inclined surface. The numerical model reproduces the presence of the shear layer and the correct sign alternation; however, the distribution is more diffuse and less concentrated. In particular, the shear layer in the numerical field appears thicker and less intense, suggesting a possible attenuation of the strongest gradients.

In the +35° case, the intensity of vorticity in the experimental field increases, and the region characterized by significant values extends further into the upper part of the domain. The presence of stronger gradients along the panel is clearly visible and consistent with the more pronounced flow deviation observed in the previous analysis. The numerical model correctly identifies the location of the shear layer but again represents it with a smoother and less concentrated distribution. The regions of high vorticity appear more blurred and less fragmented compared to the experimental field.

In both configurations, away from the panel, the numerical field appears more stratified and uniform, whereas the experimental result shows greater local variability, particularly near the free surface. This difference

is consistent with the time-averaged nature of the RANS approach, which tends to filter out smaller-scale rotational structures and provide a more continuous representation of the flow field.

Overall, the vorticity comparison confirms that the numerical model is able to reproduce the location and general nature of the shear layers generated by the panel but tends to underestimate their local intensity and smooth out thinner rotational structures. The discrepancies are therefore most evident in regions of strong gradients, where the experimental flow exhibits higher complexity and turbulence modelling reveals its limitations.

6. CONCLUSIONS

This study provided a controlled laboratory investigation of the flow–structure interaction mechanisms induced by inclined photovoltaic panels installed within a free-surface channel, reproducing near-neutral boundary layer conditions through dynamic similarity. By combining Particle Image Velocimetry (PIV) measurements with Reynolds-Averaged Navier–Stokes (RANS) simulations, the work enabled a comprehensive characterization of both mean flow behaviour and turbulence-related quantities.

The experimental results clearly indicate that panel inclination represents the dominant parameter governing flow reorganization within the analysed domain. While increasing discharge leads to a uniform amplification of velocity magnitudes, it does not significantly alter the qualitative structure of the flow field. In contrast, variations in panel inclination produce substantial modifications in the vertical redistribution of momentum, in the development of shear layers, and in the spatial extent of recirculation regions.

The mean velocity fields reveal that increasing the inclination angle enhances velocity gradients along the panel surface, promoting stronger flow deviation and more pronounced wake formation. Streamline analysis confirms the development of recirculation zones above and downstream of the panel, whose spatial extension grows with increasing inclination. These geometric effects are consistently reflected in the turbulent quantities.

Turbulent kinetic energy (TKE), vorticity, and Reynolds stresses demonstrate that larger inclination angles intensify turbulence production and momentum exchange processes. The concentration of high-TKE regions and strong shear layers in proximity to the panel indicates that geometry-driven velocity gradients constitute the primary mechanism responsible for turbulence generation. The coherent trends observed across all analysed quantities confirm the internal

consistency of the experimental dataset and provide a physically robust interpretation of the flow behaviour.

The comparison with the RANS numerical model shows good qualitative agreement in reproducing the mean velocity distribution and the location of the principal shear layers. The model successfully captures the general structure of the wake and the redistribution of momentum induced by panel inclination. However, in regions characterized by strong gradients and localized turbulence production, the numerical solution tends to smooth the flow field and underestimate the spatial extent and intensity of vortical structures. These discrepancies are consistent with the intrinsic limitations of time-averaged turbulence modelling approaches, which inherently filter small-scale fluctuations.

From a broader perspective, the results highlight the critical role of geometric configuration in governing flow redistribution and turbulence dynamics around photovoltaic modules. Since airflow modification directly influences near-surface exchange processes, such geometric effects may have relevant implications for microclimatic conditions in agrivoltaic systems. The findings therefore provide a reference framework for future investigations aimed at optimizing panel layout and inclination in order to balance aerodynamic, structural, and environmental performance.

Overall, this work establishes a solid experimental benchmark for the analysis of flow behaviour around photovoltaic arrays and offers a consistent basis for further developments, including the adoption of more advanced turbulence modelling strategies and the extension of the investigation to different geometric configurations and operating conditions.

REFERENCES:

1. Barron-Gafford, G. A., Pavao-Zuckerman, M. A., Minor, R. L., Sutter, L. F., Barnett-Moreno, I., Blackett, D. T., Thompson, M., Dimond, M. A., Gerlak, A. K., Nabhan, G. P., & Macknick, J. E. (2019). *Agrivoltaics provide mutual benefits across the food–energy–water nexus in drylands. Nature Sustainability,* 2, 848–855.
2. Barron-Gafford, G. A., Murphy, P., Salazar, A., Lepley, K., Rouini, N., Barnett-Moreno, I., et al. (2025). *Agrivoltaics as a climate-smart and resilient solution for midday depression in photosynthesis in dryland regions. Sustainable Agriculture,* 3, 32.
3. Campana, P. E., Stridh, B., Hörndahl, T., Svensson, S.-E., Zainali, S., Lu, S. M., Zidane, T. E. K., De Luca, P., Amaducci, S., & Colauzzi, M. (2024). *Experimental results, integrated model validation, and economic aspects of agrivoltaic systems at northern latitudes. Journal of Cleaner Production*, 437, 140235.
4. Charonko, J. J., & Vlachos, P. P. (2013). *Estimation of uncertainty in PIV measurements. Measurement Science and Technology,* 24(6), 065301.
5. Holmes, P., Lumley, J. L., & Berkooz, G. (1996). *Turbulence, coherent structures, dynamical systems and symmetry*. Cambridge University Press.
6. Li, M., Chen, T., Ma, S., Liu, F., He, Y., Feng, Z., Yao, Z., & Xiao, J. (2025). *Wind field characteristics of photovoltaic arrays based on wind tunnel tests. Solar Energy*, 300, 113867.
7. López, J., Parnás, A., & Cataldo, P. (2019). *Wind tunnel experiments on ground-mounted photovoltaic solar panels. Revista Ingeniería de Construcción,* 34(2), 115–126.
8. Pope, S. B. (2000). *Turbulent flows. Cambridge University Press.*
9. Raffel, M., Willert, C. E., Wereley, S. T., & Kompenhans, J. (2018). *Particle image velocimetry: A practical guide (3rd ed.). Springer*.
10. Stull, R. B. (1988*). An introduction to boundary layer meteorology. Springer.*
11. Thum, C. H., Okada, K., Yamasaki, Y., & Kato, Y. (2025*). Impacts of agrivoltaic systems on microclimate, grain yield, and quality of lowland rice under a temperate climate. Field Crops Research*, 326, 109877.

12. Wang, J., Hu, W., Wen, Y., Zhang, F., et al. (2025). *Dust deposition characteristics on photovoltaic arrays investigated through wind tunnel experiments. Scientific Reports,* 15, 1582.
13. Weselek, S., Ehmann, A., Zikeli, S., Lewandowski, I., Schindele, S., & Högy, P. (2021). *Agrivoltaic system impacts on microclimate and yield of different crops within an organic crop rotation in a temperate climate. Agronomy for Sustainable Development*, 41, 59.
14. Wilcox, D. C. (2006). *Turbulence modeling for CFD (3rd ed.). DCW Industries.*